João Pedro Coias Vieira

Bachelor of Sciences in Micro and Nanotechnologies Engineering

Optical coherence tomography for the evaluation of vulnerable plaques with nanoprobes

Dissertation submitted in partial fulfillment
of the requirements for the degree of

Master of Science in
Micro and Nanotechnologies Engineering

Adviser: Doctor Mariana Torres Carvalho, Research Engineer,
International Iberian Nanotechnology Laboratory

Co-adviser: Doctor José Ricardo Ramos Franco Tavares,
Full Professor, NOVA University of Lisbon

Examination Committee

Chair: Prof. Dr. Rodrigo Ferrão de Paiva Martins
Rapporteur: Prof. Dr. Rui Alberto Garção Barreira do Nascimento Igreja
Members: Prof. Dr. José Ricardo Ramos Franco Tavares
Dra. Mariana Torres Carvalho

FACULDADE DE
CIÊNCIAS E TECNOLOGIA
UNIVERSIDADE NOVA DE LISBOA

December, 2019

Optical coherence tomography for the evaluation of vulnerable plaques with nanoprobes

This document was created using the (pdf)LaTeX processor, based on the "novathesis" template[1], developed at the Dep. Informática of FCT-NOVA [2].
[1] https://github.com/joaomlourenco/novathesis [2] http://www.di.fct.unl.pt

"Pedras no caminho? Eu guardo todas. Um dia vou construir um castelo."

— Nemo Nox

Acknowledgements

I wish to express my thanks to all those who have in any way allowed this thesis to come true.

Firstly I want to thank Dr. Mariana Torres Carvalho of the International Iberian Nanotechnology Laboratory, for letting me be part of her working group and having believed in me and my abilities.

Thank you also for the theme of the work, that has always attracted me, which most of the time managed to help overcome the difficulties that arose. I am also grateful for the freedom of action that was decisive for this work to contribute to my personal development. To my friend and lab partner Sara Fonseca, for all the help and company during all this months which allowed us both to grow.

I would also like to thank Prof. José Ricardo Ramos Franco Tavares, from the Faculty of Science and Technology of the NOVA university of Lisbon, the conversations that, one way or another, always gave important practical results.

I also appreciate the simple, correct and scientific way that has always approached our working meetings without never allowing the discouragement to settle in.

To Dr. Carlos Galvão Braga at the Cardiology Department of Hospital of Braga and Dr. Victor A. Jimenez Diaz team at the Cardiology Department of Hospital Alvaro Cunqueiro of Vigo, thank you for your permission and availability in conducting tests at each of their facilities using the clinical OCT systems and also the exchange of impressions which were extremely helpful to me.

To Andrea Cruz, research fellow at INL, for all the help and discussions regarding the biotinylation of the antibodies.

To Sara Abalde-Cela and Alexandra Teixeira, from the microfluidics group at INL, for all the help and availability in the synthesis of the gold nanostars.

To all the amazing people that I've met and were part of my stay at INL, in Braga, thank you so much for all the great and fun moments, and for always pushing me to challenge myself. Without you guys it would have been way more tedious.

Um agradecimento a todo o corpo docente do DCM, em especial ao Prof. Rodrigo Martins e à Prof. Elvira Fortunato sem os quais este curso não existiria. Aos professores Pedro Barquinha e Daniela Gomes e às responsáveis pelos laboratórios no CENIMAT Alexandra Gonçalves e Sónia Pereira, um muito obrigado por toda a ajuda que me deram, não só nesta tese como em tantos outros projectos e pelo bom espírito de equipa que se nota por todo o CENIMAT. Tornaram o meu primeiro contacto com o mundo da investigação deveras inesquécivel.

À Inês e Pina, minhas amigas de sempre e para sempre, agradeço as longas conversas, as melhores aventuras e a preocupação com que sempre tiveram comigo.

Ao grande Success, Açoriana, Ferreira, Castelo, Mariana e Luís, que venham daí muitos mais convívios. Vocês são grandes!

Aos meus maravilhosos amigos Marta, Alexandra, Diogo, Mariana, Rodrigo e Pedro pelos anos de amizade e partilha de momentos, obrigado por tudo.

E, finalmente agradeço à minha família, que sem eles nunca teria conseguido chegar onde cheguei:
Aos meus avós, pelo infindável carinho. Ao meu avô, professor e amigo, que tanto me acompanhou.
À minha tia, tanto pelo apoio, como pelos miminhos e carregamentos que ajudaram sempre a encurtar a distância onde quer que tenha estado.
Ao meu pai pela atenção e sólida formação dada e à minha mãe que decerto teria ficado muito feliz por este momento.

Os meus eternos agradecimentos.

A eles dedico este trabalho.

Abstract

This project aims to design and develop a robust diagnostic intravascular imaging system for *in situ* detection of labeled coronary vulnerable plaques, consisting in the integration of targeted nano-probes with a novel protocol for IV-OCT (Intravascular optical coherence tomography) imaging, to analyze anatomical and molecular features of plaques with high precision, sensitivity and specificity.

This approach to molecular imaging using IV-OCT focuses primarily in the investigation of possible contrast agents. Thus, this study is composed, in addition to their functionalization, by the comparison of gold nanostars and Poly(n-butyl cyanoacrylate) (PBCA) microbubbles as possible candidates. The results show a special attention to PBCA microbbubles being that they exhibited the most noticeable scattering effect leading to more valuable imaging.

A three-dimensional structured tissue-mimicking phantom was also presented for use in IV-OCT. The phantom was fabricated from a PDMS matrix and titanium dioxide additive, capable of producing a wide variety of scattering densities. We describe the fabrication, characterization and IV-OCT imaging of these phantoms and demonstrate their utility in functionalization with two types of contrast agents.

Finally, commercial Endothelium-targeted PBCA microbubbles (Fujifilm Visualsonics) were tested using clinical IV-OCT systems in *post mortem* human arteries allowing its unequivocal location in the sample. The results present the first steps towards adding to the routinely used IV-OCT a new functionality.

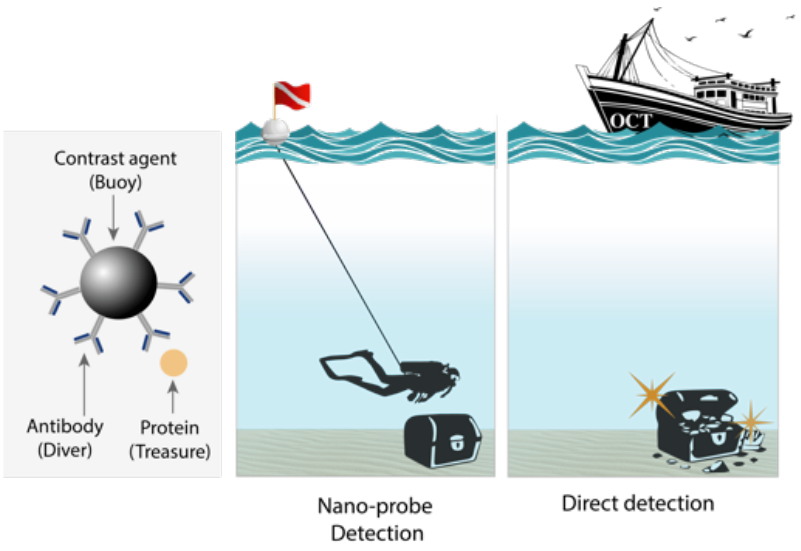

Dissertation goals: Contrast agent-aided molecular imaging process. The direct visualization of endogenous disease markers in the body is nonexistent as it is not possible to distinguish from surrounding tissue using OCT imaging. The proposed method rests in the use of exogenous contrast agents with the specificity to bind to the target in question. Image designed in Adobe Illustrator®.

Keywords: Gold nanoparticles, Molecular Imaging of atherosclerosis, Nanotechnology, OCT intravascular imaging, PBCA microbubbles, Targeted nano-probes.

Resumo

Este projeto tem como objetivo delinear e desenvolver um sistema robusto de diagnóstico por imagem intravascular para a deteção *in situ* de placas coronárias vulneráveis, que consiste na integração de nano-sondas endereçadas a bio-marcadores característicos da doença com um novo protocolo de imagem intravascular por tomografia de coerência ótica (IV-OCT). Conseguindo assim analisar características anatómicas e moleculares das placas com alta precisão, sensibilidade e especificidade.

Esta abordagem de imagem molecular usando IV-OCT concentra-se principalmente na investigação de possíveis agentes de contraste. Assim, este estudo é composto, para além sua funcionalização, na comparação de nanoestrelas de ouro e microbolhas de poli(n-butil cianoacrilato) (PBCA) como possíveis candidatos. Os resultados apresentam as microbolhas de PBCA em foco, dado que estas exibem um efeito de dispersão mais perceptível, levando a imagens mais valiosas.

É importante salientar que um simulador físico de tecidos biológicos (Phantom) foi igualmente apresentado para uso em IV-OCT. Este material, criado para mimetizar algumas das propriedades óticas das artérias humanas, foi fabricado a partir de uma matriz de polidimetilsiloxano (PDMS) na qual foram dispersas nanopartículas de dióxido de titânio, sendo possível obter uma ampla variedade de densidades de espalhamento da luz. A fabricação, caracterização e imagem por OCT dos referidos phantoms é descrita, bem como a demonstração da sua utilidade na funcionalização com dois tipos de agentes de contraste.

Por fim, destaca-se que microbolhas de PBCA comerciais (Fujifilm Visualsonics) foram funcionalizadas com anticorpos contra células endoteliais e testadas usando sistemas clínicos de OCT em artérias humanas *post mortem*, permitindo a sua localização inequívoca na amostra. Os resultados apresentam os primeiros passos em direção a acrescentar uma funcionalidade extra ao IV-OCT utilizado rotineiramente na cardiologia intervencional.

Palavras-chave: Imagem Intravascular de OCT, Imagem Molecular de Aterosclerose, Microbolhas de PBCA, Nano-sondas direcionadas, Nanopartículas de Ouro, Nanotecnologia, Simuladores de tecido.

Contents

List of Figures

List of Tables

ε	Extinction coefficient ($M^{-1}cm^{-1}$)
Abs_{280}	Absorbance at 280 nm
Abs_{400}	Absorbance at 400 nm
C	Concentration (M)
L	Optical path length (cm)
lc	Coherence length

ACS	Acute coronary syndromes
CVD	Cardiovascular diseases
FD-OCT	Fourier domain optical coherence tomography
GNST	Gold nanostar
IV-OCT	Intravascular optical coherence tomography
LDL	low-density lipoproteins
LSPR	Localized surface plasmon ressonance
MB	Microbubble
MCOCT	Molecular contrast-based optical coherence tomography
MWCO	Molecular weight cut-off
NIR	Near-infrared
OCT	Optical Coherence Tomography
VE-cadherin	vascular endothelial cadherin

Cardiovascular diseases (CVDs), the leading causes of death in the western world, are now gaining ground also in developing countries [1] . Enormous efforts are being put into raising awareness, research and treatment of the spectrum of CVDs, including acute coronary syndromes (ACS) and stroke. A study by the World Health Organization, the World Heart Federation and the World Stroke Organization into Cardiovascular Disease Prevention and Control state that: "from the two-thirds of all deaths in the world, which belong to non-communicable diseases, almost 50 % are from CVDs alone" [2] . Furthermore, CVDs should not only be recognized as a significant cause of morbidity but also as a major economic burden and an obstacle to global development and sustainability[3].

Although our knowledge of disease progression leading to plaque build-up in atherosclerosis has increased over the last few years, our ability to predict future events is still insufficient. Different imaging technologies are being developed to visualize various features of vessel walls that could indicate the onset of acute cases such as ACS and stroke, but there is yet no single technique that provides a robust prognosis of CVDs [4].

In this context, Optical Coherence Tomography (OCT) has rapidly evolved from its initial ophthalmological applications into a plethora of medical fields, like interventional cardiology. Since its development in 1991, at the Department of Electrical Engineering Computer Science on the Massachusetts Institute of Technology (MIT) [5], the many advances in OCT not only strengthened the vast applicability of the technology, but also continue to bring enthusiasm to applications that may still be discovered. Considering that OCT is a minimally invasive imaging method upholding high penetration depth and spatial resolution, when compared to other imaging techniques [6].

Due to the technological shift in 2003 from the nowadays-called time-domain OCT to the fourier-domain, the rapid imaging of the intervascular medium was finally attainable and several clinically approved imaging systems have appeared soon after. Nevertheless, with all the many advances, OCT still has room for innovations, not only on hardware but also in software and optical systems. Other techniques can be implemented in the same system, providing multidimensional information to the OCT data. For instance, recent techniques such as Doppler [7] and Polarization sensitivity OCT [8] have brought additional contrast to clinical images and the ability to visualize and quantify blood flow; while supercontinuum fiber laser sources are being used to obtain high-resolution images [9] and computational adaptive optics where suggested as the algorithm of choice for an improved aberration correction [10].

However, a clear and unmet clinical need remains: the identification of metabolic changes in the tissue. Despite OCT significance in the diagnosis of clinically important diseases and unprecedented resolution of vessel microstructural features, imaging of disease biomarkers is still elusive. OCT is foremost a morphology imaging technique and many diseases do not promote a significant change in the tissue so the OCT can observe. Therefore, to visualise these morphological alterations, it is necessary the use of contrast agents. However, trough the best of our knowledge, there are no contrast agents that can couple OCT contrast with biological targeting [11], and thus, there are no clinical

approaches to image disease biomarkers in biological processes using this technology. This project fits in this contest to improve current diagnostic capabilities of intervascular OCT as a clinical tool. We proposed to attain that goal combining OCT with molecular imaging. Thus, the specific objectives of this work were:

- Synthesis and characterization of contrast agents able to produce significant OCT signal;
- Optimization and development of a tissue simulating platform for rapid testing of contrast agents;
- Synthesis of functionalized nano-probes for targeting arteries;
- Integration of targeted nano-probes with IV-OCT imaging, in an innovative protocol to analyse anatomical and molecular features within post mortem human arteries.

In addition to putting into practice the hard skills learned during the course of Micro and Nanotechnologies, this work greatly influenced the development of soft skills that helped substantially in the different practical aspects of this thesis. Namely in designing user interfaces, optimizing graphical outputs, and delivering specific data analysis tools using MATLAB programming language, complemented with custom designed illustrations/pictograms using the vector graphics editor (Adobe Illustrator®).

Chapter 1

Introduction

1.1 Overview of atherosclerosis

Cardiovascular disease (CVD) is a generic term applied to a large number of conditions affecting both the heart and blood vessels. It is the leading cause of death in the world and continues to be a significant burden for all society [1]. It mainly includes coronary heart diseases (blood vessels supplying the heart muscle), cerebrovascular diseases (blood vessels supplying the brain) and peripheral arterial diseases (blood vessels supplying the arms and legs). Above all, the most common reason for all these disorders is the build-up of fat deposits inside of the artery walls, a process referred to as atherosclerosis (Figure 1.1).

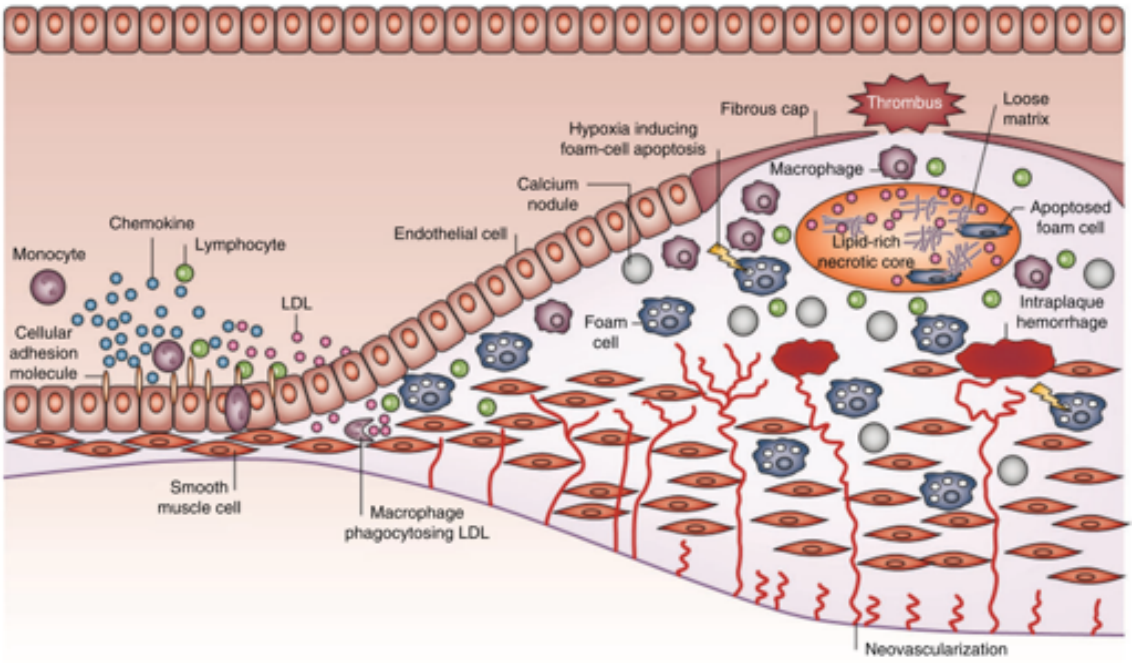

Figure 1.1: Atherosclerotic plaque development. The monocytes can adhere and pass through the endothelium, where they transform into macrophages and ingest the foreigner low-density lipoproteins, becoming foam cells that contribute to the narrowing of blood vessels (Retrieved from Ref [12]).

At the beginning of the atherogenic process, patches of arterial endothelial cells begin to express on their surface selective adhesion molecules [e.g.: selectin, vascular cell adhesion molecule 1 (VCAM-1) and intercellular adhesion molecule 1 (ICAM-1) [12]] that bind with various classes of leukocytes. This cell dysfunction process does not occur naturally, it is a response to lesions on the endothelium wall at predisposed regions (e.g. near branch points and along the inner curvature of the arteries) [12] due to risk factors such as hypertension, smoking and high cholesterol level. At these sites, low-density lipoproteins (LDLs) go through the endothelium and promote an inflammatory response that leads to endothelial dysfunction. Once adhered to the endothelium, the leukocytes penetrate the

intima (innermost layer of the artery) and differentiate into macrophages that scavenge for the foreigner LDLs. However, once the macrophages uptake reaches a limit point, the inflammatory process no longer remains under control and a chronic process takes place. Macrophages with an excess intake of lipids turn into "foam cells" and agglomerate in the interior of the vessel walls, forming an atheroma or plaque. These plaques are the basis for the atherosclerotic process and lead to the narrowing of the blood vessels (stenosis). Although atherosclerosis on its own is rarely fatal, the rupture and thrombosis of the atheroma account for all the acute cases such as heart attacks and strokes. The assessment of these vulnerable plaques, that have a high risk of rupturing, remains a challenge in cardiology [4] . After all, these plaques are mainly diagnosed accounting the morphology of the vessel walls (i.e. high luminal stenosis and thin cap). However, it is acknowledged that the risk of rupture depends more on the plaque composition rather than its anatomy [4].

1.2 Current diagnosis methods

It is impossible to proclaim that a perfect imaging solution exists since it is not guaranteed that it will be optimal in every diagnostic situation. Different systems perform optimally in different types of clinical practice settings. As so, several criteria are considered when comparing alternative imaging methods for plaque characterization - namely, the resolution, imaging depth and sample intrusiveness (Figure 1.2).

The following sections will overview OCT in cardiology, comparing with other techniques and finally the basic principles of this imaging method.

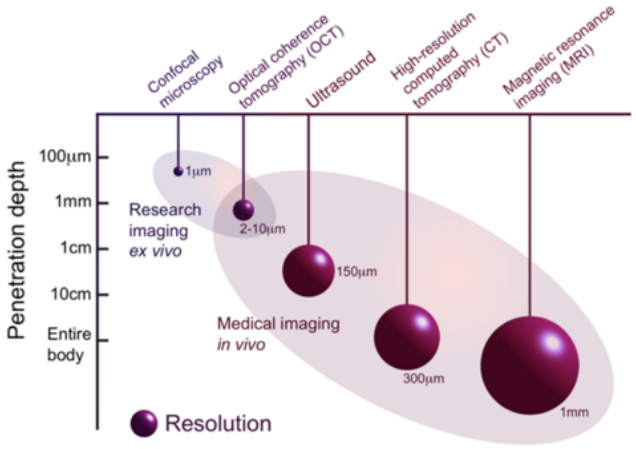

Figure 1.2: Comparison between different imaging techniques in terms of imaging depth and resolution. Retrieved from the website of the Optical and Biomedical Engineering Laboratory,"Introduction to OCT", University of Western Australia.

1.2.1 Currently used methods in cardiovascular diseases

In the diagnosis of coronary heart disease, the first common approach for the medical doctor is coronary angiography [4]. This exam detects sites of luminal stenosis for further treatment such as stent placement using an intravascular contrast agent and X-ray imaging. Angiography is used primarily to localise the region where there is a blood

flow blockage, however, it does not have enough resolution to visualize specific structures in the artery wall. In this sense, Optical coherence tomography (OCT) has been a very promising imaging solution in distinguishing the composition of plaque structures, fitting between conventional optical microscopy (confocal and fluorescent microscopy) and ultrasound (Figure 1.2) [6]. Whereas methods such as magnetic resonance imaging (MRI) and intravascular ultrasound achieve greater imaging depths, allowing the diagnosis of larger areas, OCT far exceeds in terms of resolution. A typical OCT allows for spatial resolution up to 10 µm [6], and its ability to perform in vivo images is greatly appreciated. In the case of cardiovascular imaging, a catheter-based OCT works as a minimally evasive solution, allowing the detailed visualization of the arterial layers and the accurate assessment of plaque features in small arteries (0.5 to 1.5 mm) [13]. As so, IV-OCT has proven to be a promising imaging modality in obtaining cross-sectional tomographic vascular images [14].

1.2.2 Principles of OCT

The imaging process in OCT can be viewed as the light equivalent of ultrasound, measuring the "echoes" of light backscattered by the sample to build an image. In intravascular OCT (IV-OCT), a fibre optics cable (catheter) transmits the light and collects the reflection inside an artery, while rotated and pulled across its length. There are two main approaches to obtain OCT data: time-domain and Fourier-domain methods. Originally, OCT was developed as an interferometric technology where the spatial information was obtained depending on the time delay between the sample and a reference beam. As so, a very basic OCT setup, depicted in Figure 1.3, closely resembled a Michelson interferometer.

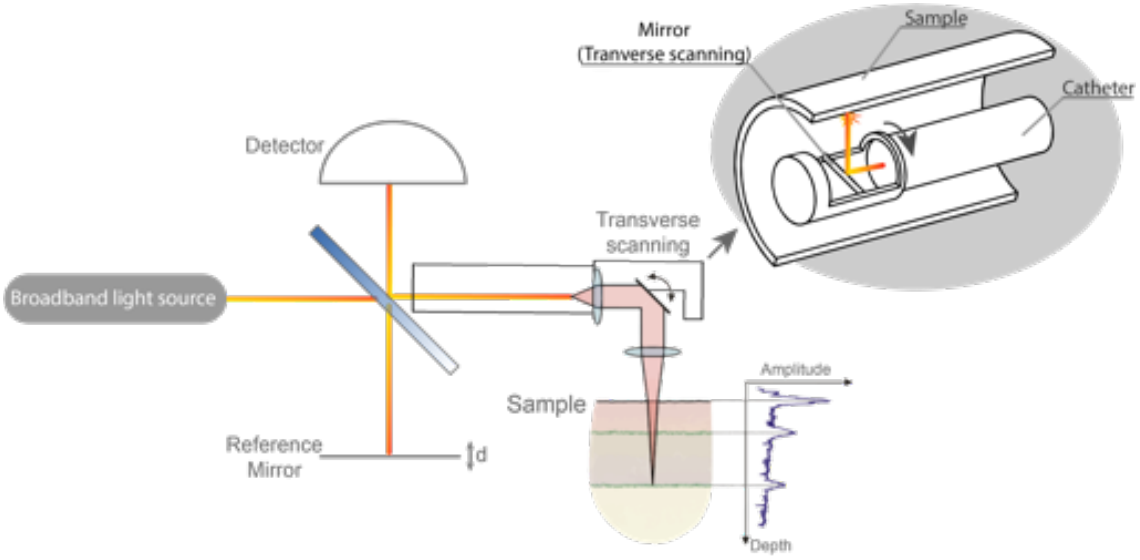

Figure 1.3: Depiction of the basic interferometric OCT setup. Catheter scheme and positioning within a sample. Image designed in Adobe Illustrator®.

The Michelson interferometer is a common configuration for optical interferometry. A

beam splitter divides the light beam emitted from a light source, so that half goes into a reference path (mirror) and the other half to the sample. The beams are reflected back in both arms of the interferometer and recombined before being detected by a sensor, producing an interference effect.

However, it is essential to note that this interference, meaning constructive/destructive interaction between the two light beams, only occurs when the optical path on both arms of the interferometer is almost equal (difference smaller than the coherence length of the light source). Thus, by moving the reference arm, the location of a certain feature in the sample can be assessed with the resolution of the coherent length of the source. Moreover, a interference pattern is obtained depending on the mirror position, corresponding to the specific reflection characteristics of a feature in the sample at that position (optical path distance).

Performing a pre-determined sweep of the reference mirror positions, which correspond to an imaging depth range, one axial (Z) scan is obtained. This is also referred to as an amplitude scan (A-scan) and corresponds to a map of the different reflections within one axial direction (Figure 1.4). Additionally, it is possible to obtain a cross-section of the sample by joining multiple A-scans from directions transverse to the light beam (B-scan). Finally, by combining multiple B-scans a 3D model of the sample is attained.

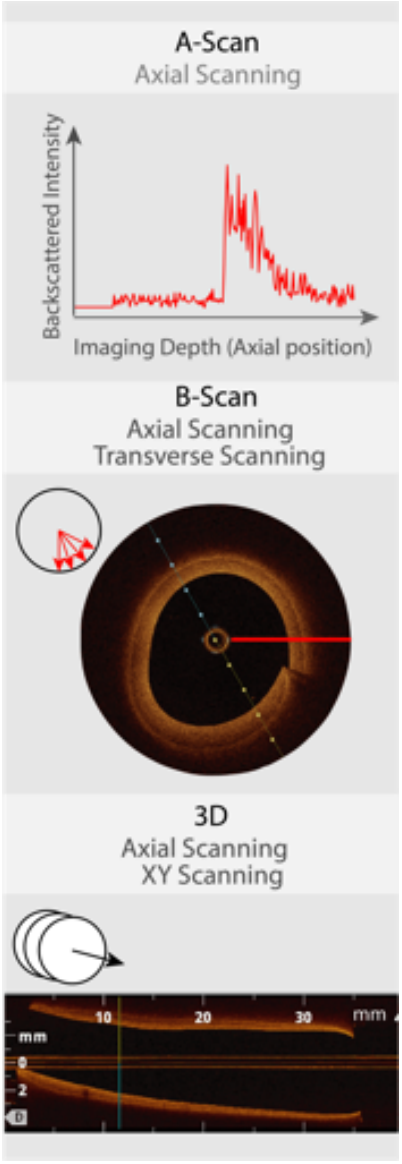

Figure 1.4: OCT scan Types. A-scan, B-scan, tomographic reconstruction (3D reconstruction and sectioning). Image designed in Adobe Illustrator®.

It is important to note that the coherence length of the light source (lc) determines the axial resolution. Oversimplifying, the coherence length describes the distance over which two beams maintain a constant phase difference hence interference is observed between these two beams. For this reason, broadband light sources, which have low-coherence, are used to better differentiate the reflections from individual structures in the path of the beam.

However, in 2003, different studies have demonstrated that the shifting from Time-domain methodology to Fourier-Domain improved the detection sensitivity by several orders of magnitude [15]. As so, current devices no longer use the conventional OCT

setup, they obtain measurements in the frequency space, though the same principle of interferometry remains. In Fourier-Domain OCT (FD-OCT) the reference arm of the system is fixed and the measurements are wavelength-dependent. In general terms, the intensity of light hitting the detector (I) that defines the OCT output signal is given in terms of the resulting electric field, E, in equation 1.1 [16].

$$I \approx \frac{cn\varepsilon_0}{2}|E|^2 \tag{1.1}$$

Where c is the speed of light in vacuum, n is the refractive index of the medium and ε_0 the vacuum permittivity. Nevertheless, the resulting electric field, E, corresponds to an interaction between the electrical component of the optical field from the sample arm (E_s) and the electrical component from the reference arm (E_r), in the form(1.2):

$$|E|^2 = |E_s|^2 + |E_r|^2 + 2|E_s||E_r|cos(\omega\tau) \tag{1.2}$$

Where ω corresponds to the source optical frequency and τ to the delay caused by the optical path difference between the sample and the reference arms. In the Time-domain OCT, the frequency ω is fixed and the τ changes with the movement of the reference mirror. The cosine term then yields a maximum received signal when $\tau = 0$, i.e., the optical path distance difference between the reference and sample arms is zero. As long as the movement of the mirror is known (position × time), interferograms such as the one observed in Figure 1.3, of the light intensity versus mirror displacement I(τ), can be obtained. In contrast, the Fourier-Domain OCT fixes the reference mirror position, maintaining the optical path difference constant and measuring the intensity spectrum in the frequency domain I(ω), which is then converted to a measurement equivalent to the Time-Domain using the inverse Fourier transform. A detailed discussion of the numerous practical aspects of optical coherence tomography and mathematical formulations is beyond the scope of this work. Additional information on this topic can be found in pertinent works already reported [16–18].

1.3 How tissue material appears in OCT

In OCT, light from the source is attenuated (scattered and absorbed) as it passes through the tissue sample. The strength of backscattering, the main imaging process in OCT, provides a mechanism to differentiate structures and is influenced by the different constituents in the biological medium (cells, organelles and fibres) [19]. Absorption, on the other hand, occurs mainly in pigments, such as haemoglobin and melanin and water [20]. It limits on how much the OCT can measure, and it depends on the source wavelength and the tissue characteristics. Therefore it is important to note that, in order to achieve greater imaging depths in tissues, absorption must be the lowest possible (ignoring scattering effects). Therefore, as different biomolecules absorb certain wavelengths more readily than others do, a diagnostic/therapeutic spectral window is always defined when working with light-tissue interactions [21]. Light at wavelengths in the near-infrared (NIR) spectral region, from 1100 to 1350 nm, correspond to low blood absorption (oxy-

and deoxyhemoglobin) [21]. To this end, the central wavelength of the IV-OCT light source is generally chosen in the range of 1250 to 1350 nm [22] . Moreover, the size, shape, density of different scattering structures and their refractive index predetermine the character of light propagating in tissues. Allowing for a morphologic assessment of the interior of vessel walls and a preliminary study of their composition.

1.4 OCT perspectives

As referred, plaque vulnerability seems to depend more in composition than morphology. As a result, diagnosis with OCT falls short due to the inability of detecting distinctive biological traits, such as disease chemical markers. The ideal imaging method should report not only the volume of plaques within the artery walls but also plaque biological characteristics. Thus, to enhance the capability of this imaging system would be to combine OCT with molecular imaging. This hybrid optical imaging approach exploiting the high-resolution and excellent penetration depth of OCT with a smart optical contrast agent could dramatically enhance imaging capabilities. A contrast agent that can elicit molecular contrast grants the possibility of tracking the distribution of biochemical components in samples [23]. Thus, allowing trailing diseases evolution in patients and trial subjects. There are two ways by which molecular contrast–based OCT (MCOCT) procedures can be utilized to image a particular chemical or protein distribution within a target:

- Directly detecting the chemical or protein due to its innate contrast capabilities;
- Attaching a contrast agent to a vehicle that recognizes and binds to the chemical or protein in question.

In the work of Yang et al. [24], an example of this first method is presented (Direct detection). The distribution of a plant protein (phytochrome A) is achieved from pairs of consecutive OCT A-scans. This specific protein can reversibly switch between two states with different absorption maxima accordingly to the wavelength of an externally exposed light. In this type of technique, the contrast agent is endogenous to the target organism. However, it is not very often that we find the required protein or chemical that also performs well as a contrast agent. Moreover, even if in principle it should be possible to genetically-engineer animal models to express these proteins for biomedical research applications, simpler and quicker diagnosis methods are required.

For the second method presented of MCOCT imaging, the molecular target is highlighted by what we can refer has marker “buoys”. An exogenous contrast agent that is efficiently distinguished by the OCT can be functionalized so that it ties to the particular chemical or protein of interest. As a figure of speech, imagine a diver as an antibody that finds and binds to the wanted protein (Treasure) (Figure 1). Attached to him is the buoy that pops up on the water surface, warning the boats that a diver will soon float. The only detectable signal by means of OCT is the buoy, from which by now the position can be used to co-localize both the diver and the protein sought for. This method has a very significant advantage, since it can be used to recognize and map chemicals or protein that

are otherwise undetectable directly by OCT in the target tissue, as long as it is possible to design a contrast agent that is visible in the OCT system.

1.5 Molecular contrast agents: Micro and nanoparticles

Optical molecular imaging is rapidly expanding using new exogenous molecular probes [25]. Different types of contrast agents are being studied for OCT [4], however, mainly four categories apply: scattering, modulating, absorbing and plasmon resonant probes. For the first category, scattering, the most common particles are metals and other particles with a refractive index significantly different from the tissue. Scattering is an optical phenomenon that depends on size of the particles and the wavelength of the light (as the case of Raleigh and Mie scattering), but it generally increases with the magnitude of the refractive index difference between the particle and the surrounding media. The microbubbles studied in this work are an example of this category.

Since OCT detects light backscattered from refractive index mismatches it was forecasted that gas-filled microbubbles would produce contrast in OCT. In fact, the first study of the effects of microbubbles was presented in 2002 by Barton *et al.* [26]. Initial tests in phantoms demonstrated that MB can be used as contrast agents for OCT [26]. Since the microbubbles increased the attenuation coefficient of blood a great advantage in the use of MB arised and became the main focus of such contrast agents. The enhanced visualization of the blood vessel lumen, because after all the optical properties of blood are very similar to the surrounding tissue [26].

More recently studies have focused on the quantitative assessment of the MB contrast in well-controlled systems that accurately mimic tissue optical properties and flow conditions [27]. However, the study of targeted imaging using MB in OCT has been lacking. While microbubbles are being readily used with ultrasound systems to the point that there are already FDA approved commercial contrast agents.

In the second case, modulating probes modify one observable property in situ, like the case of the plant protein presented by Yang et al. [24]. While background remains constant, the alternation between different observable states allows for an improved detection. Which, in this case, depends mostly on the comparison of two consecutive images. The absorbing probes case is based on the local attenuation due to absorption [25]. Instead of focusing in the local optical changes, the effect of absorbing probes is noticed in deeper structures of the tissue, as reduced backscattering intensity is observed in these regions. In this case, the contrast agent promotes a shadow effect, as it absorbs most of the light passing through, structures that are behind it do not receive enough light to be visualised. Finally, plasmon-resonant probes address the trend of reducing the size of the probes while maintaining a sufficient scattering cross section. This is accomplished by the use of metal nanoparticles that exhibit a phenomenon called surface plasmon resonance (SPR). The collective excitation of electrons promotes an increased scatter effect in the nanoparticles, and it depends on the material, size, and structure of the particle.

Chapter 2

Materials and Methods

Additional information and the detailed protocols regarding this section can be consulted in Annex I and II.

2.1 Synthesis and Characterization of the contrast agents

2.1.1 Gold Nanostars (GNST)

The detailed protocol on all the steps for the synthesis of gold nanostars can be found in annex I. Gold nanostars were synthesised using a method modified by the microfluidics group at INL, of a previously reported seed-mediated growth by Pandian Senthil Kumar *et al* [28]. Already synthesised, citrate stabilized 15 nm spherical gold nanoparticles, produced with the Turkevich method [29] were previously coated with polyvinylpyrrolidone (PVP) and used as gold seeds for the following GNST synthesis (Au@citrate@PVP - 2×10^{-3} M). For the typical seed-mediated growth, 2.5 g of polyvinylpyrrolidone (PVP MW = 10,000 g mol^{-1}) were dissolved in 25 mL of N, N'-dimethylformamide (DMF, MW= 73.09 g mol^{-1}), using an ultrasound sonicator, until all was dissolved. Following, 99.15 µL of an aqueous solution of chloroauric acid ($HAuCl_4$ - 0.1268 M) was added to the solution under magnetic stirring. During the 1 min of mixing, the solution got lighter in colour from the reduction of $Au_3{}^+$ to $Au_1{}^+$. Following, 317 µL of Au@PVP seeds (2×10^{-3} M) were quickly added to the solution still under stirring. The reaction flask was left covered with aluminium foil to protect it from light. Within 2 h, the color of the solution changed from brownish to a very dark blue/grey, indicating the formation of gold nanostars in solution. The resulting gold nanostars were washed (5500 rpm, 60 min) with IPA to stop the reaction and remove excess reactants.

To prepare codified gold nanostars, 4 µL of ammonium hydroxide (NH_4OH- 29%), 2 µL of an ethanol solution of mercaptoundecanoic acid (MUA – 3.75 mM) and different fluorescence dyes (10^{-4} M) were added to 2 mL Eppendorf's containing 0.8 mL of a 1 mM solution of the previously synthesised gold nanostars. Although only one of the fluorescence dye was used in the further experiments (Nile Blue - NB), different batches of GNSTs were also coded with toluidine blue (TB). After continuous magnetic stirring for 2 hours, each one of the solutions passed through 2 washing steps composed of an ultrasound bath for 2 min and centrifuge at 2500 rpm for 30 min. Each time re-dispersing in IPA until 1 mL. The resultant gold nanostars where characterized using a FEI Quanta 650 FEG scanning electron microscope and further absorbance measurements were taken in a Perkin-Elmer LAMBDA 950 UV-VIS-NIR Spectrophotometer. The size distribution was preformed using the imaging processing package Fiji for ImageJ.

2.1.2 PBCA microbubbles

Poly(n-butyl cyanoacrylate) (PBCA) microbubbles where kindly provided by Prof. Twan Lammers' (ExMI, Helmholtz Institute for Biomedical Engineering - Germany) group. Two different varieties of PBCA microbubbles where received. Initially, PBCA microbubbles where obtained in Triton-X without any surface active groups. This microbubbles varied

in size from 1.8 to 2.5 µm and where produced in professor Twan lammers group [30]. The second batch consisted of VeVo MicroMarker® Target-Ready contrast agents (from Fujifilm Visualsonics) made by Bracco Research SpA. These where used for further biofunctinalization procedures. Using the preparation protocol from Fujifilm Visualsonics, VeVo MicroMarker® Target-Ready contrast agents were reconstituted. Initially 0.7 mL of saline was injected into the microbubble flask with a 21G ½" needle attached to 1 mL syringe. The syringe was then removed letting the vial vent with the needle still injected. Finally, the needle was removed completely, and the vial gently agitated for 10 seconds. The synthesis process of both batches can be analyzed in detail in reference [30].

2.2 Functionalization

2.2.1 Immobilization of gold nanostars on PDMS surface

The immobilization method was performed using a modification of the previously reported work of Nguyen Ba Trung, *et al.* [31]. The formerly synthesised coded (Nile blue) gold nanostars were deposited on a poly(dimethylsiloxane) (PDMS) substrate based on electrostatic interactions. Substrates were first activated with oxygen plasma for 2 min. On this step, a mask in the form of another PDMS slab or adhesive tape, was used to cover a specific area of the substrate, in order to adhere the nanoparticles on the exposed side. Following a washing step with ethanol, the substrates were dried with N_2 gas. The cleaned substrates where then immersed in different silane solutions. Initially the silane crosslinker used was (3-Aminopropyl)trimethoxysilane (APTMS, sigma Aldrich) at 1%(v/v) and 8.33%(v/v) ethanol solution. While in the end it was switched to (3-Aminopropyl)triethoxysilane (γ-APTES, sigma Aldrich) at 1%(v/v). The substrates where immersed for 5 or 15 min in each of the solutions. From here on, the substrates were immediately cleaned with ethanol and water to remove any residual silane molecules. Then the masks were removed. Next, the samples were annealed at 80°C for 1 hour and 30 minutes. Finally, the substrates are immersed on the colloid gold nanostars solution, previously prepared, again for 1h and 30 min and thoroughly rinsed with deionized water. The substrates are well dried and placed in the oven for an annealing step of 1 hour at 80 ºC. A Zeiss LSM780 confocal microscope with 34 simultaneous confocal fluorescence counting channels was used to access the distribution of the coded nanoparticles.

2.2.2 Biofunctionalization

The detailed protocol of the biofunctionalization process can be found in annex II. **Tissue**. -80 °C frozen human carotid was obtained for immunohistochemistry, these samples are considered in a protocol with INMLCF (Instituto Nacional de Medicina Legal e Ciências Forenses). The artery sections where cut crosswise into two pieces, defrosted and fixed in acetone at -20 °C. Following, all the samples were washed three times in PBS.

Biotin-labelling of Unconjugated Goat Anti-rabbit IgG antibody. Immunoglobulin (IgG) molecules (Novex by Life technologies TM, Lot 62-10-092817) where first biotinylated using Thermo ScientificTM EZ-Link TM Sulfo-NHS-LC-Biotin (sulfosuccinimidyl-6-[biotin-amido]hexanoate) (MW: 556.59 ;Lot. Nr. A39257 21335). The devised protocol was based on the user's guide for the EZ-Link TM product (MAN0016133, Pub. Part No.21611855). Initially a 10 mM solution of the biotin reagent was prepared in 500 µl of ultrapure water. Following, a 60-fold molar excess of biotin (10 µl) was taken from the prepared solution and added to 3.75 mL of a saline solution containing 250 µg of the stock antibody. The solution was then incubated at room temperature for 30 min. The resulting antibodies where further purified using Amicon Ultra-0.5 Centrifugal Filter units with a Ultracel-100 regenerated cellulose membrane and a nominal molecular weight limit of 100 k at 2000 rpm for 2 min. The protein concentration on different steps of the filtration was obtained with a Nanodrop 2000 microvolume spectrophotometer from Thermo Scientific.

Immunohistochemistry procedures. **Primary immunohistochemistry** of rabbit anti-VE-Cadherin IgG antibodies (Thermo Fisher, Code: V1514-200UL, Lot. 016M4804V) was performed overnight (8h) at 4°C. The primary antibody solution was prepared according to the recommended values described by the supplier. From a PBS buffer solution containing 1% of bovine serum albumin (BSA), 4 mL where mixed with 20.4 µl of anti-VE-Cadherin IgG. The positive artery samples where then immersed in this solution and left incubating overnight. The negative samples where immersed in a PBS blocking solution with 3% BSA and also left overnight. After this process the samples were washed three times in PBS. The VeVo MicroMarker microbubbles where reconstituted from the respective vial as referenced in section 2.1.2 and the preparation protocol from Fujifilm Visualsonics was again used for further biofunctionalization. Using a 21G ½" needle with a 1 mL syringe 0.3 mL of the filtered biotinylated Goat Anti-rabbit IgG (20 µg) where injected into the microbubble vial (total volume of 1 mL). The functionalized contrast agent solution was then gently agitated by hand for 1 min and left to rest at room temperature for 15 minutes.

The **secondary immunohistochemistry** step was finally performed by transferring the fully assembled microbubble solution to an Eppendorf with the positive artery section, adding 2 mL of saline to top the required 3 mL necessary for the experiment. Joining the secondary antibody (Goat Anti-rabbit IgG) with the primary antibody (rabbit anti-VE-Cadherin IgG). The incubation step was performed for 1 hour at 4°C while agitating and was followed by three washes in PBS. The artery sections where supended in a saline solution.

2.3 Phantom design

2.3.1 Scattering agents

The TiO_2 nanoparticle synthesis was performed in CENIMAT/i3N at NOVA University. The hydrothermal-microwave assisted method was slightly adapted from a previously reported work [32]. A CEM Discover SP Microwave Synthesiser was used for the hydrolysis of a solution containing 2 mL of a titanium precursor (Titanium (IV) isopropoxide, sigma Aldrich), 5 mL of an acid catalyst (Nitric acid, sigma Aldrich) and 55 mL of ethanol. The solution was first prepared under magnetic stirring until all reactants were fully mixed. Only then where 20 mL transferred to a Pyrex reaction vessel and placed in the microwave synthesiser. Next a predefined program was set for 1 hour and 15 min with the following set points: 200 ºC, 100 PSI and 100 W. Further commercial TiO_2 powders where used in later phantoms. The Characterization of the TiO_2 powders was performed on a FEI Quanta 650 FEG electron microscope.

2.3.2 PDMS nanocomposite phantoms

SYLGARD® 184, a two-part Polydimethylsiloxane (PDMS) kit from DOWSIL (formerly DOW CORNING, Michigan, EUA) was used as the matrix material for the phantoms. The kit is composed of a base (PDMS) and a curing agent (reactive). The PDMS phantoms were produced in a two-step approach. First, the titanium dioxide particles with a weight percentage of 0.6% to 3% (according to which layer) are introduced into the base resin without the reactive. Each of the mixtures was initially hand mixed and then placed in the ultrasounds for at least 4 h. Next, the required amount of the PDMS composite was transferred to a separate container were the curing agent was added in a ratio of 10:1. The final compound was mixed and poured into the moulds were each layer is left to cure for 1 h at 65 °C. The composite material was synthesized by simple mixing, without any treatment to both the matrix PDMS and titanium dioxide nanoparticles. It is important to note that the compositions of the phantoms here presented were based and modified from the article in Ref [33], which uses alumina as the scattering agent. Furthermore, as in the work by Bisaillon *et al.* [33], we decided not to use anything to induce absorption in the phantoms.

2.4 OCT

Two different clinical IV-OCT systems where used *in situ*, thanks to the partnership with Dr. Victor A. Jimenez Diaz team at the Cardiology Department of Hospital Alvaro Cunqueiro (University Hospital of Vigo, Spain) and Dr. Carlos Galvão Braga at the Cardiology Department of Hospital de Braga (2CA-Braga, Portugal). Pullbacks from University Hospital of Vigo were acquired from a Lunawave coronary imaging console with a Fastview coronary imaging catheter (Terumo Corporation, Ashitaka, Japan), hereafter referred to as "Terumo-OCT". While pullbacks from Hospital de Braga were acquired using the ILUMEN FD-OCT system from Abbott (formerly St. Jude Medical, St. Paul, MN) with a C7 Dragonfly catheter.

Chapter 3

Results and Discussion

3.1 Phantom characterization

3.1.1 Scattering agents

To introduce optical scattering, white titanium dioxide (TiO_2) powders were added to the phantoms. These were chosen as potential scattering agents for the optical phantoms as they are a easily synthesized material and even commercially available at low-cost.

Commonly used as a whitening pigment in paint, sunscreens and even food couloring, TiO_2 powders are often used to fabricate OCT phantoms even tough their refractive index (2.3) greatly exceeds those from most often biological structures [34]. However, in the context of this research, the emulation of tissue optical properties was mainly oriented on how light interacts with the phantom and not the rigorous mimicking of all the optical properties of common tissues. As so the main concern was obtaining different magnitudes of scattering scales by mixing different concentrations of TiO_2.

Initially a small amount of TiO_2 powder was synthesised at CENIMAT/i3N using a hydrothermal-microwave assisted method. After further development of the phantoms, commercial food grade TiO_2 was purchased. A comparison of both samples was taken using scanning electron microscopy. The hydrothermally synthesized TiO_2 exhibited irregular morphology throughout all the sample with particles smaller in size than those seen in the commercial powder. However, the commercial powder is composed of roughly spherical nanoparticles with sizes ranging from 70 to 300 nm.

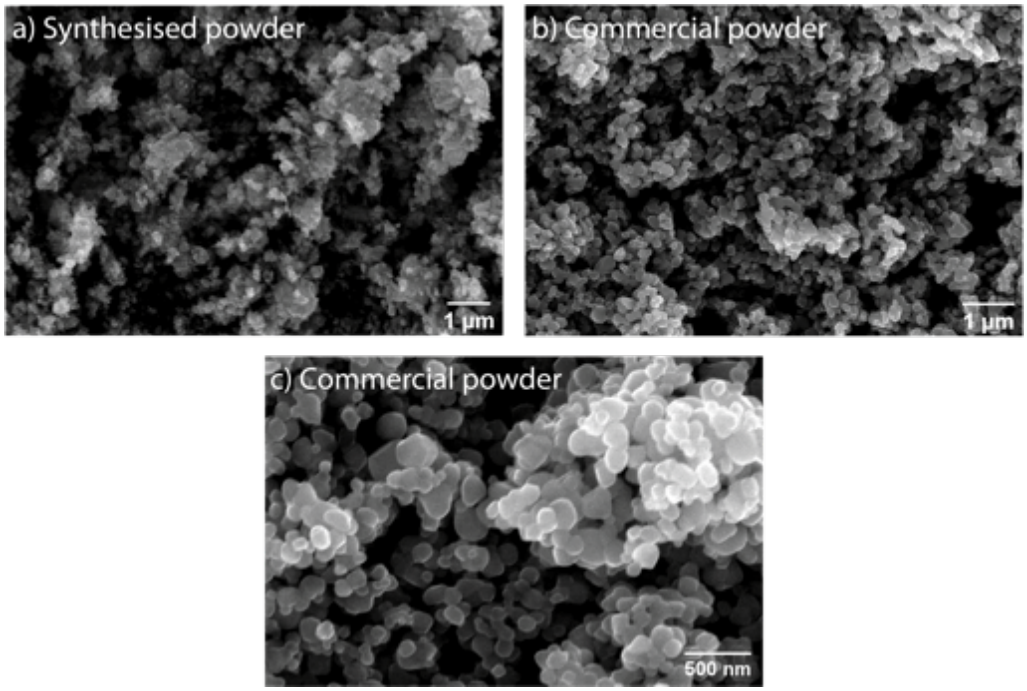

Figure 3.1: Scanning electron microscopy (SEM) images of the hydrothermally synthesised TiO_2 powders and the commercially available ones: (a) TiO_2 powder synthesised at CENIMAT/i3N; (b and c) Commercial food grade TiO_2 in different magnifications.

The size and dispersion of these TiO_2 particles were very similar to sub-/extracellular structures that dissipate light in typical tissues. Actual biological tissues are more complex than a homogeneous distribution of identical spherical particles or even randomly shaped ones. A mixture of large and small particles may be a good approximation to describe tissue scattering properties. Figure 3.2 presents the difference between the initial stock PDMS and the turbid PDMS composite with about 0.142 % (w/w) of the synthesised TiO_2.

(a) Stock PDMS (b) Scattering PDMS

Figure 3.2: Photographs of mould casted PDMS slabs prepared with and without added scattering agents.

Once a uniform distribution of the TiO_2 powders into the PDMS matrix was achieved, the optical characterization of the different PDMS slabs, made following a rigorous protocol such that the final thickness remained similar in all measured samples, was performed and it is presented in the following section.

3.1.2 Optical characterization

Ultraviolet-visible (UV-Vis) spectra measured in transmission mode of each of the mould-casted PDMS layers (Figure 3.2) are displayed in Figure 3.3. Confirming the transparency of the stock PDMS matrix in all the recorded spectrum (350-1500 nm) with the exceptions of weak absorption peaks at around 1200 nm due to vibrations in the polyatomic CH_3 groups in the PDMS [35]. The silicone matrix obtained using the Sylgard 184 kit presents a very uniform group refractive index of about 1.4 (at a wavelength of 1.3 µm) [34] very close to common tissues. The extinction is however significantly increased with the rise in the titania content thus, when the light passes through the film, it would be more difficult for the photons to pass the diffusive film. The central wavelength of the clinical OCT systems in use ($\lambda_{OCT} = 1350nm$) is represented in the graph as a vertical red line. At this wavelength the composite PDMS with a total weight percentage of 3 % TiO_2 has about twice the amount of the extinction of the 0.6 wt% phantom. As a result, different magnitudes of scattering from each of the phantom are expected during the OCT measurements. With this in mind, a multi-layered phantom was devised in order to reproduce the structure of actual blood vessel walls.

The blood vessels are divided into three layers [33] that are composed of different types of cells:

- Intima, is the inner layer, mainly composed of endothelial cells has the middle OCT signal;
- Media, is the middle layer, composed by connective tissue and smooth muscle cells, has the lowest OCT signal ;
- Adventitia, is the outer layer, composed by fibrous tissue to provide support to the artery. It has the highest OCT signal from all the three layers.

In this work only the two innermost layers (Intima and Media) were considered for the phantom structure. The developed fabrication process only allowed the synthesis of layers with about 1 mm (Figure 3.4) and the stacking of three different layers led to non-malleable phantoms that were difficult to curve into the desired format for measurement in the OCT system. In future procedures, if necessary, the phantoms could be constructed with the help of a 3D printer, which would allow better control of the thickness of the layers.

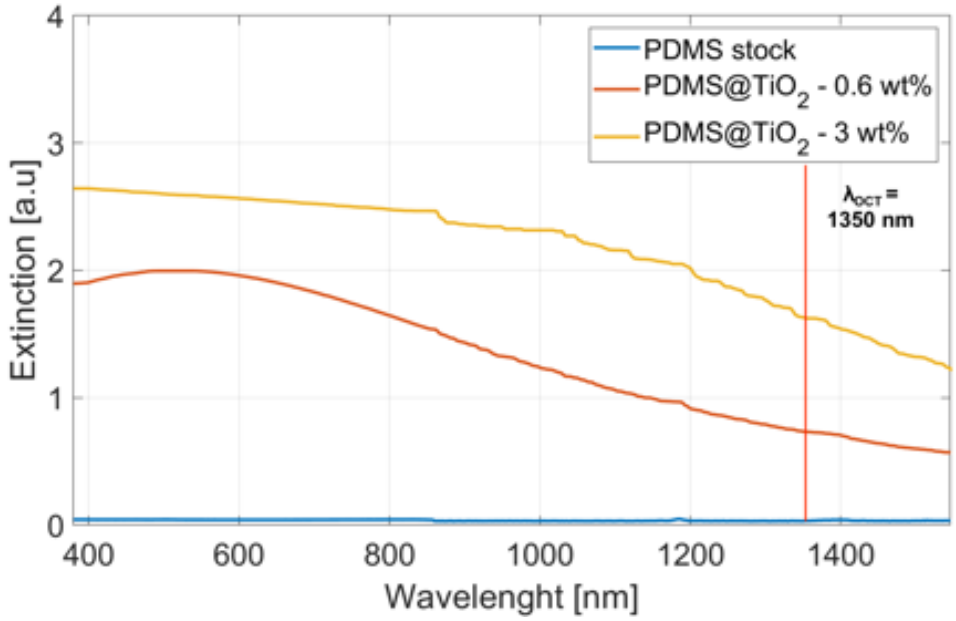

Figure 3.3: Extinction vs wavelength of stock PDMS substrate and of PDMS substrates with different concentrations of TiO_2 nanoparticles. Obtained without the cuvette on the spectrometer: Substrate adhered to the stand (Approximate thickness of 1 mm).

Figure 3.4 represents the box plots with the variation of the thickness measurements of each of the layers. The thickness measurements were performed using the image analysis software ImageJ on the images obtained in the OCT systems, considering the pure PDMS refractive index. On both of the layers the spacing between the different parts of the box indicates some degree of dispersion of the measured thickness, which expresses an heterogeneous thickness throughout the PDMS slabs.

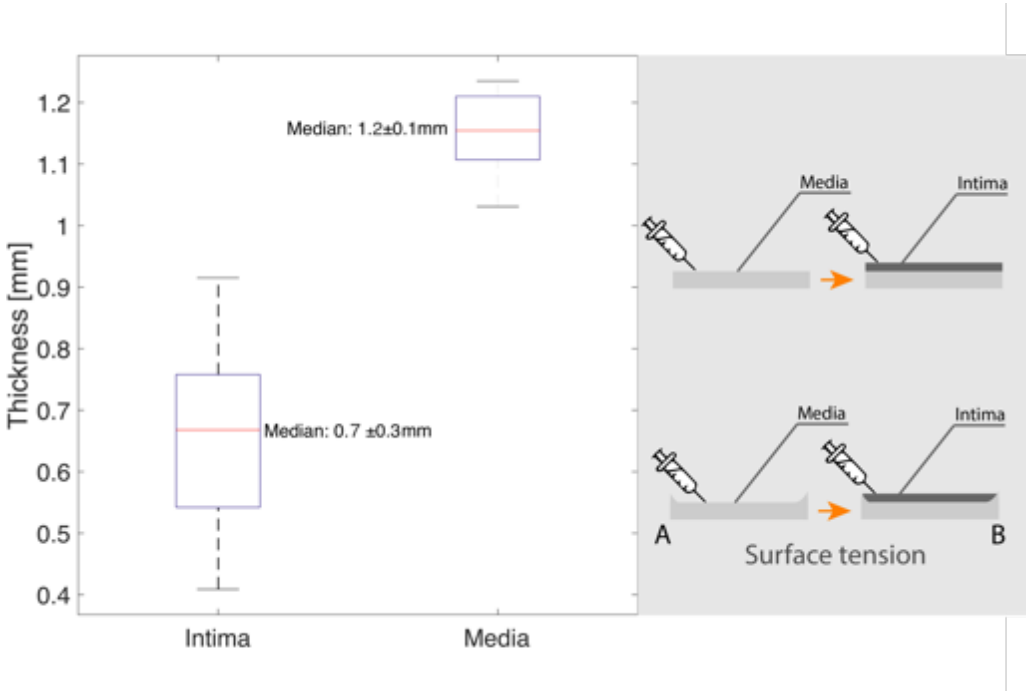

Figure 3.4: Thickness measurement distribution of each layer from optimized phantom. Surface tension causes the sides of the phantom to curve contributing to the deviations in the thickness measurement

In fact when observing the OCT cross-section of a phantom with both layers stacked (Figure 3.16) smaller thickness of the intima and larger in the media are noticed on the edges. This thickness distribution is mostly due to tensions with the mould during the fabrication process. When the first layer is poured and spread the surface tension with the mold walls creates a receding contact angle which when cured creates a protrusion in the slabs (Figure 3.4-A). In turn, when the second layer is transfered the inverse inprint occurs (Figure 3.4-B). This features in the phantom lead to the overall variations in the measured thickness.

3.1.3 Synthesis and characterization of contrast agents

The synthesised gold nanostars where optically and morphologically characterized. Figure 3.5 shows the UV-Vis spectra of the 15 nm gold nano seeds (blue) used in the synthesis of the gold nanostars whose spectra is observed in red.

Extensive literature is found on both the synthesis and optical characteristics of gold nanostars [36, 37]. In all this reports two different localized surface plasmon ressonance (LSPR) modes are described, corresponding to different locations of the near electric field in the nanoparticles (central core (seed) and tips). Surface plasmons (SP), which involve collective oscillations of electrons confined to a metal/dielectric boundary, can interact strongly with incident electromagnetic fields [38]. Their behavior is directly influenced by several parameters including the structure, shape, and size. This ultimately affects the optical properties of the nanoparticle, which can be observed via its UV-Visible absorption.

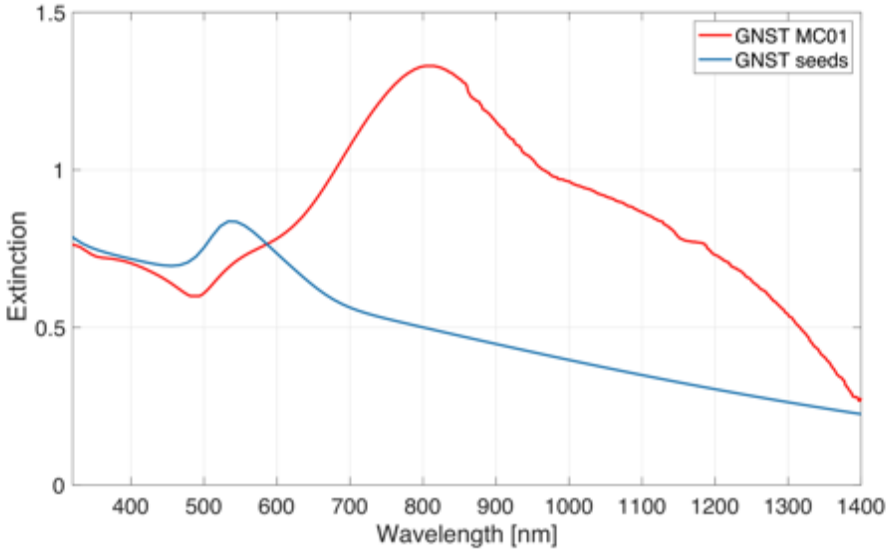

Figure 3.5: Extinction spectra of the Au nanoparticle seeds and following gold nanostars from 380 - 1400 nm.

The prepared gold nanostars (GNST) display a well defined plasmon band with a maximum absorbance at 810 nm (tip mode), together with a weaker shoulder around 555 nm corresponding to the core mode as shown in Figure 3.5. The GNST seeds have only one band as expected at around 555 nm. The effect of the tip mode LSPR presents interesting possibilities as a large enhancement of the electric near field and light concentration occurs near this wavelength. A so-called "antenna effect"[39]. Moreover, a study by Abhitosh Kedia and Pandian Senthil Kumar [36], showed that is also possible to precisely tune the gold nanostars LSPR peaks by controlling the shape of the tips. Sharper tips lead to an enhanced red-shift of the tip mode LSPR (Annex III.1) which can then be tuned to a region near the central wavelength of the OCT imaging where a very strong interaction occurs, enhancing the backscattered light.

Moreover, UV-Vis spectra of the GNST allowed to obtain their concentration in the measured solution. At a wavelength of 400 nm organic molecules and the surface plasmon resonance of the gold nanoparticles have only minor influence. The absorbance is mainly due to interband transitions of gold and therefore can serve as a robust measure of the concentration [40]. As so, using the Beer-lambert law the concentration of an absorbing species can be related to the absorbance (Abs_{400}), as it has a linear relationship (Equation 3.1) [41].

$$Abs_{400} = \varepsilon \times L \times C \tag{3.1}$$

Where ε is the extinction coefficient ($M^{-1}cm^{-1}$), L is the optical path in cm, and C the concentration in molarity. Assuming that a extinction of 1.2 at 400 nm corresponds to a complete gold reduction ($C = 0.5$ mM) [42] and that the optical path corresponds to 1 cm, the extinction coefficient of gold nanoparticles ($\varepsilon = 2.4{\times}10^3 M^{-1}cm^{-1}$) is initially obtained.

From here on, using the same equation, the calculation of the molar concentration of the GNST was possible to attain. This values are then used in conjunction with the morphology characteristics to obtain the value of particles/ml.

The morphological characterization by transmission electron microscopy is shown in Figure 3.6. The images were analyzed using Image J and the diameter of the gold nanostars was measured. For that, in image containing several GNSTs (> 100 particles), an automated algorithm was used to draw an elipse around each star and the diameter was measured. The obtained distribution is shown in Figure 3.6 for two different batches, named SA56 and MC01.

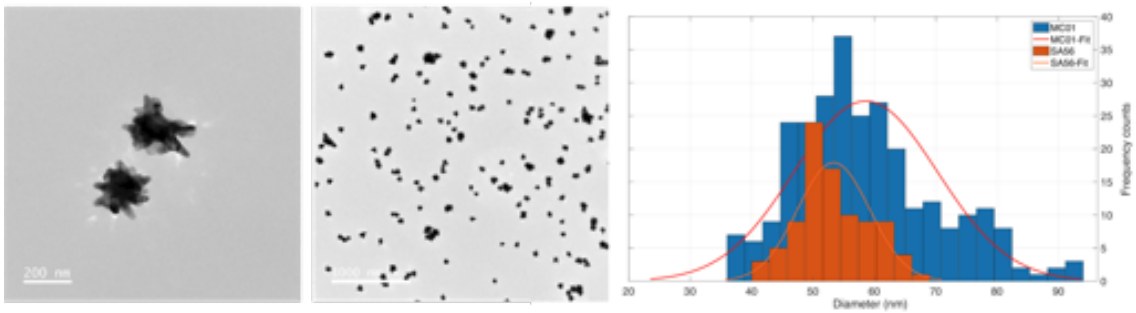

Figure 3.6: TEM images of MC01 batch of gold nanostars. Diameter distribution for MC01 (58 ± 19 nm) and SA56 (53 ± 9 nm) samples.

The GNST appeared to be relatively monodispersed with a mean diameter of 58 nm (MC01). As an example of the variation during the synthesis process of the GNST, the size distribution of a diferent batch of GNST is presented (SA56). Even though the exact procedure was done in both batches a slight variation in size is observed.

Table 3.1: GNST morphological characterization and particle count.

Sample	Mean Diameter [nm]	Concentration [mM]	Particles/mL
MC01	58.58 ± 19.46	0.302	3.9×10^{10}
SA51	53.25 ± 9.78	0.555	7.2×10^{10}

The ensuing analysis refers to Figure 3.7 where the recorded fluorescence emission of the nile blue dye, adsorbed to the GNST surface, is present. A laser scanning microscope was used both for the fluorescence characterization of the coded GNST, characterizing it's spectral emission properties, and the spatial mapping of said nanoparticles in further functionalization studies. The inset in Figure 3.7 represents the confocal fluorescence maps under illumination with a 633 nm laser. In each pixel of the fluorescence confocal image, the emission spectrum was recorded using the lambda mode of the microscope. In Figure 3.7 the integrated spectral information associated to the delineated region in the recorded image are shown in the spectral range of 400 nm to 750 nm.

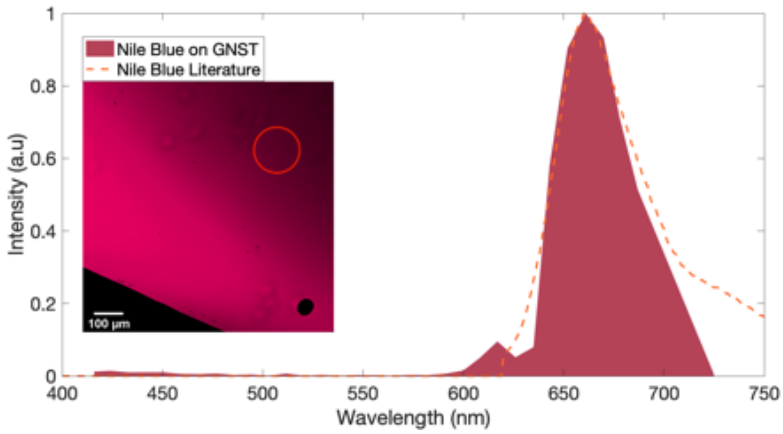

Figure 3.7: Emission spectra of Nile blue dye at 5% power of a 633 nm laser.

3.2 Functionalization

3.2.1 Immobilization of GNST on the surface of PDMS

The silanization of glass substrates for the immobilization of gold nanoparticles has been for a while an efficient method of creating platforms for photonic devices, microelectronics and biosensing [31]. In this, the well-established interaction between negatively-charged gold colloids with ionic double layer and the positively-charged amino groups is exploited. Coupling agents like amine-terminated silanes, link the inert glass and colloid gold nanoparticles using this interactions. In this work the same immobilization technique is applied to PDMS substrates. The entire procedure is represented in Figure 3.8. A selected region in the surface of the PDMS phantom was initially treated under an oxygen plasma in order replace the silane (Si–CH_2) groups with silanol (Si–OH) groups, which can then react with one end of the selected amine-terminated silane.

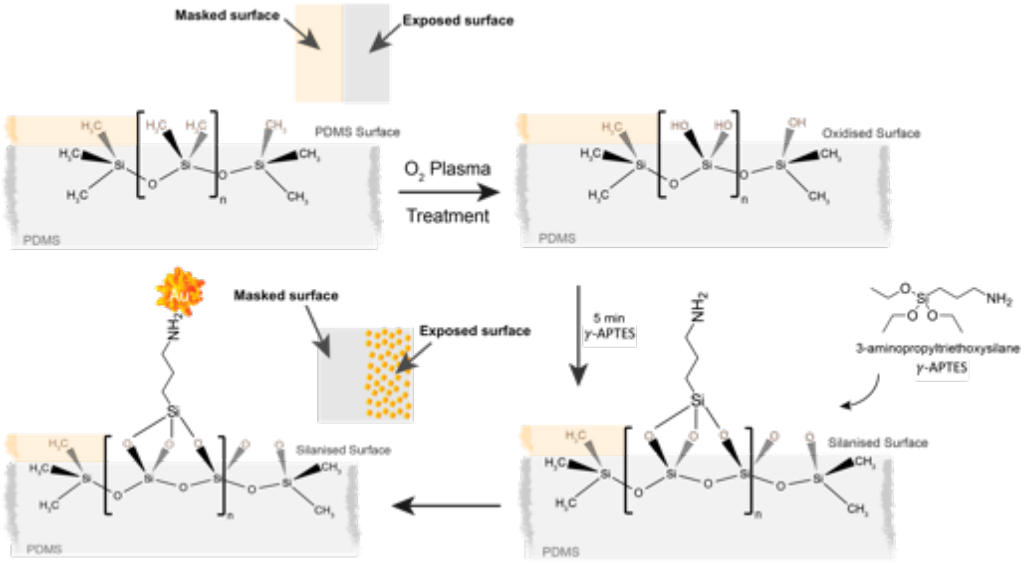

Figure 3.8: Schematic of the GNST immobilization process. Image designed in Adobe Illustrator and MolView®.

The activation of the exposed PDMS surface creates a hydrophilic surface which allowed to easily evaluate if the used mask managed to create two different sections in the phantom. The PDMS is then immersed into the silane solution, where two different immersion times were tested (5 and 15 min). This step was crucial for the following deposition of the GNSTs, since for immersion times over 5 min no nanoparticles managed to get attached. To confirm the deposition of the GNST, a confocal fluorescence microscope was used to detect the nile blue coated GNST.

A confocal fluorescence microscopy image of the resulting un-/functionalized surface of the PDMS is present bellow (Figure 3.9). This results were obtained after the optimization of the GNST immobilization using an ethanol solution with 8.33%(V/V) APTMS silane. Three different channels were used when analyzing the samples. A transmission channel obtained through a transmission camera in the setup. A second reflection channel set to detect any reflected light from the sample with the same wavelength as the laser in use. And finally a fluorescence channel which detects the wavelengths that compose the nile blue emission spectrum (Figure 3.7). In a confocal setup the reflection channel was used to make sure that the fluorescence signal was indeed coming from the surface of the PDMS, since the majority of the reflection of the used laser is at this interface between the two different materials (air/PDMS).

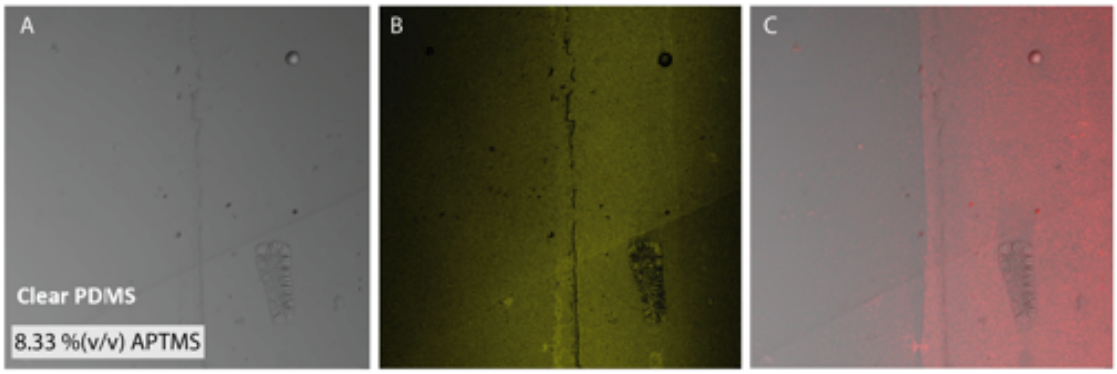

Figure 3.9: Confocal microscope images of functionalized stock PDMS. A)Transmission image, B) Reflection image, C) Transmission plus fluorescence.

In Figure 3.9-C an interface is clearly visible between a region where the fluorescence signal is null (covered side) and a side where the GNST are evenly distributed trough the surface. Following, the same process was preformed for the scattering PDMS slabs and the results are presented bellow (Figure 3.10). Although the successful padronization was also achieved in this substrates another effect was noticeable. The GNST accumulate in certain regions of the phantom which leads to the clusters observed in the fluorescence image. This result is believed to be due to the added titania nanoparticles in the PDMS matrix which create porous-like structures that trap GNST. Furthermore two different silane reagents were used for the immobilization technique APTMS and APTES. Initially the plan was to follow the procedure reported by Nguyen Ba Trung, *et al.* [31] were a

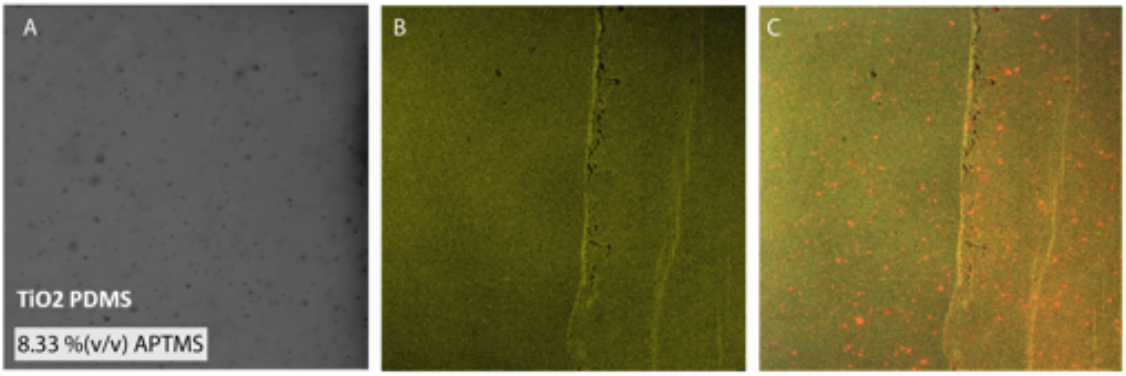

Figure 3.10: Confocal microscope images of functionalized scattering PDMS (TiO_2 PDMS). A)Transmission image,B) Reflection image, C)Reflection plus fluorescence

1%(v/v) APTES solution is used to obtain the best results. However at the beginning of this work such reagent was not available thus the similar silane molecule APTMS as used. Yet to obtain obtain the same results the final concentration of APTMS (8.33 %(v/v)) had to be higher than the reported for APTES. The results using APTES (with the exact procedure as reported in [31]) are presented in the annex IV, showing an even more uniform immobilization of the GNST.

3.2.2 Biofunctionalization

In order to fully assemble the VeVo MicroMarker target-ready microbubbles, secondary antibodies had to be initially biotinylated to facilitate the immobilization with the streptavidin in the surface of the MB (Figure II.1). This process was done with the aid of a biotinylation reagent from Thermo Scientific (EZ-Link Sulfo-NHS-LC-Biotin (lot nr. 21335, MW: 556.59)) which allows the the direct labeling of antibodies, or any other biomolecules which contain free amine groups. The EZ-link user guide was followed in order to accomplish the best possible results.

Initially to obtain an acceptable level of incorporation of the biotin in a dilute solution of antibodies a greater fold molar excess of biotin reagent was accounted for. The user guide referred a 50-fold molar excess of biotin to label 50-200 µg in 200-700 µl of buffer and considering that the antibody solution in use was even more diluted (250 µg of Ab in 3.750 mL) a 60-fold molar excess of biotin reagent was considered as a better approach.

After the correct amount of biotin reagent was determined and the labeling process was performed a process of desalting or dialysis had to be devised in order to remove excess non-reacted and hydrolyzed biotin reagent that remained in the solution. A number of dialysis membranes and size-exclusion resins were studied for this process however they did not present the resolution required for the efficient separation of the small molecules of biotin, neither an effective way to obtain high sample recoveries. As so, diafiltration devices that featured high-molecular weight cut-offs (MWCO) were the opted solution. This devices have micro-molecule permeable filters with the correct MWCO that separates immunoglobulins (>150kDa) from small proteins, peptides and even vitamins such as

Biotin (244 Da).

Additionally, in order to assess if the biotinylation process actually worked, the quantification of the IgG/Biotin concentration was carried out comparing the absorbance at 280 nm with a standard BSA calibration curve whose concentration is known.

This way, differences in the biotin concentration from the beginning of the process when compared with the filtered un-reacted biotin could indicate the efficiency of the process.

As so, during the filtration process aliquots of 15 µL from different phases where kept in a separate container and labeled for the protein quantification. Namely aliquots from the initial biotin solution, the initial antibody solution, the solution with the antibodies and biotin right after the labeling process, the concentrated solution (kept in by the permeable filters), and finally the filtered solution which should in principle only be composed of the small un-reacted biotin molecules that cross the filtration membranes.

The results of the BSA standard calibration curve and the subsequent quantification are presented in the Annex V and the following table (Table 3.2).

Table 3.2: Protein absorption quantification.

	Abs_{280}	Concentration [mg/mL]	Initial Volume [mL]	Total Concentration/Expected [mg]
Initial Biotin solution	2.2	5.3	0.5	2.7 / 2.78
Initial antibody solution	0.1	0.2	3.75	0.7 / 0.25
Antibody + Biotin	0.3	0.8	3.76	2.9 / 3.03
Concentrated	0.04	0.1	0.3	0.04 / 0.02
Filtered	0.2	0.5	0.45	0.23 / 0.06

Altough biotin on its own doesn't have absorption at the UV range (280 nm) [43] the amine-reactive group used to couple with the antibodies does [44], allowing us to use the absorption for the biotin quantification.

Upon analyzing the results in fact a reduction in biotin concentration was obtained from the initial biotin solution to the filtered solution. Which entails that some portion of the biotin molecules remained attached with the antibodies, successfully functionalizing them.

Using the initial volume of each of the tested solutions the total concentration was also calculated and compared with the quantity expected for the respective volume. In the case of the initial antibody and the filtered solution an excessive amount was clearly noticeable, even greater than the expected. This is believed to be from residual protein which interfere in the consecutive measurements. This errors could have been avoided by properly washing the detector each time a measure was taken. However in the case of the concentrated solution the excess (0.02 mg) is most likely linked to the added biotin groups adhered to the antibodies. This difference was then used to find that there are an estimated 270 biotin groups per antibody. However this difference could still be due to residual proteins in the detector, therefore to obtain a very accurate protein concentration estimation another method should be considered e.g. the bradford method.

3.3 Optical coherence tomography

One series of scattering and nonabsorbing phantoms was initially compared with stock PDMS (transparent matrix material, without introducing scattering nanoparticles).

The samples were imaged using a clinical IV-OCT system and the results are shown in Figure 3.12. Each image was selected from an cylindrical dataset (coaxial to the OCT catheter) resultant of an OCT pullback. For this initial measurements, the malleable phantoms were curved and put inside an eppendorf in a way that resembled the arteries morphology (Figure 3.11).

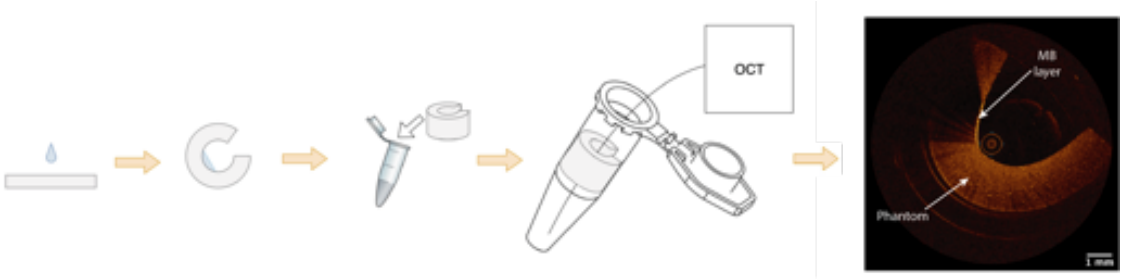

Figure 3.11: Schematics of the tissue phantom imaging. A controlled amount of the nanoprobe solution is put on a small area of the phantom. The phantom is curved (nanoprobe area inside); and put inside an Eppendorf with water. Image designed in Adobe Illustrator®.

At first, a calibration OCT pullback is performed in the same medium as subsequent images in order to correctly calibrate the software measurements based on the known diameter of the image catheter. Figure 3.12-A corresponds to said calibration in water, where poor contrast is observed due to the low intensity of scattering. However, a significant difference is observed between the stock PDMS matrix (Figure 3.12 B,D,F) and the scattering phantoms (Figure 3.12 C,E,G). As expected, the clear PDMS did not provide any signal inside it's matrix. These results can be explained from the extinction spectra of the PDMS substrates(Figure 3.3). Almost all of the light is transmitted at 1350 nm in the stock PDMS. Therefore it wasn't expected any observable features in the phantom as none of the light is being scattered back to the catheter. Only the edges of the phantom are clearly observed due to optical reflection from the interface as light encounters a refractive index change.

Contrarily, the phantoms with embedded TiO_2 particles presented an almost continuous bright background. Each of the titania nanoparticles/aggregates contributes to the scattering in the PDMS matrix. Moreover, the intensity of the backscattered light drops with penetration depth. After a certain depth, all light is mostly extinct from the path inside the phantom and the intensity of the backscattered light significantly reduces. As a result, the walls of the eppendorf, clearly visible in all stock PDMS images, become very faint. The internal structure of the phantom is vastly homogenous with negligible particle clusters.

The main goal of this work was to show the usefulness of each of the contrast agents, for this reason, a drop with a controlled amount of the contrast agents in test (GNST and

MB) was placed in the surface of the phantoms to observe their characteristic OCT signal. After careful visual inspection, it can be observed that the OCT image displays significant variation in intensity of backscattered light in specific regions of it's surface.

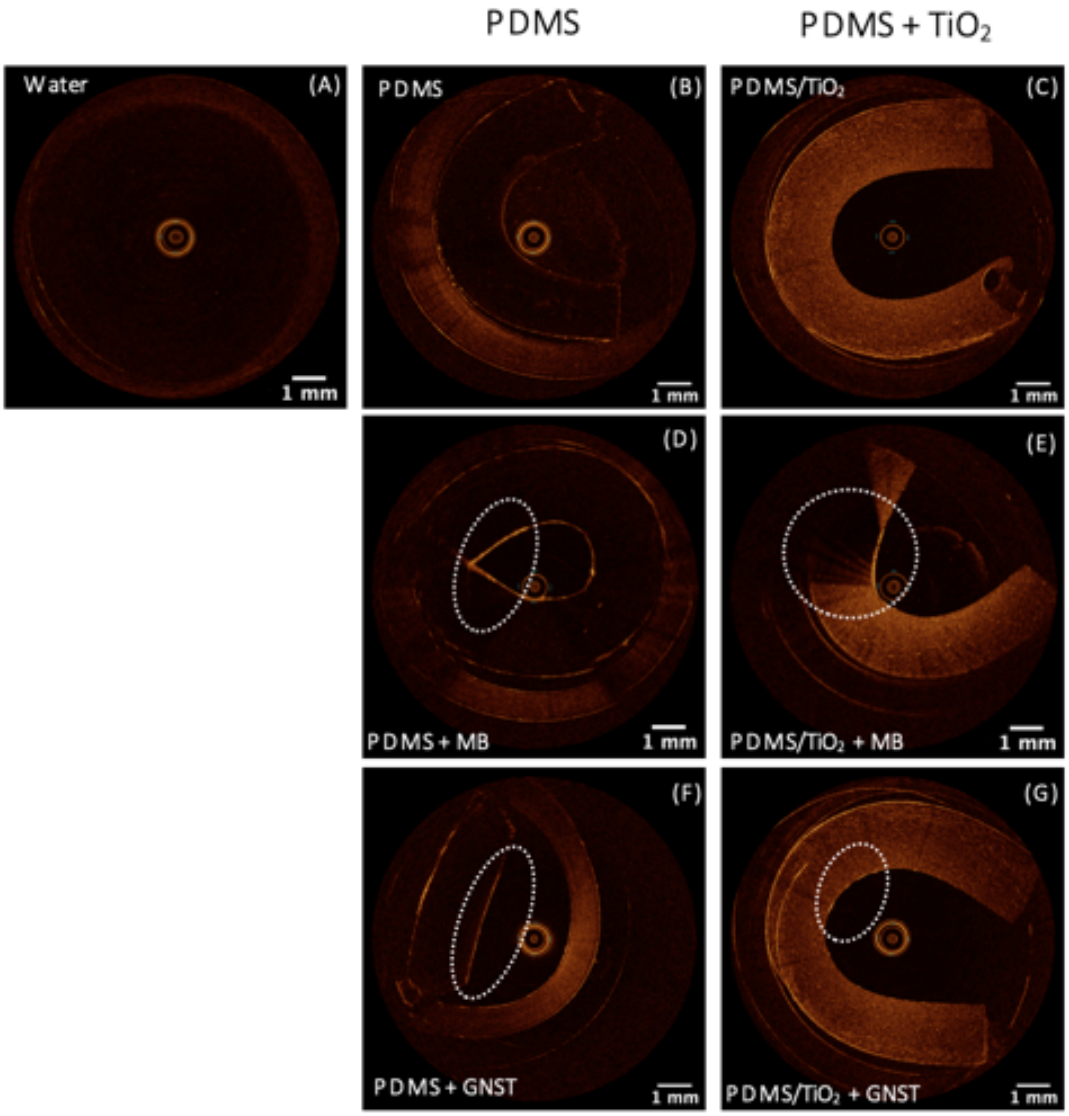

Figure 3.12: Phantom study of the contrast agents (MB: Microbubbles and GNST: Gold nanostars) for OCT. (A) Eppendorf full of water; (B) PDMS stock phantom in water; (C) PDMS phantom with dispersed TiO2 (10 mg) - Scatterer; (D) PDMS stock with dried MB spot on the surface; (E) Scatterer PDMS with dried MB spot on the surface; (F) PDMS stock with dried GNST spot on the surface and respective "shadow effect"; (G) Scatterer PDMS with with dried GNST spot.

The synthesised Gold nanostars (Figure 3.12 F,G) produced a very faint contrast in the PDMS phantoms. Notice the regions demarcated by the dashed line where the GNST are present. While GNST of this size were believed to be relatively good absorbers of near-infrared light (Figure 3.5), they did not appeared as efficient scatterers. The used

branched gold nanoparticles (GNST) may not have a suitable mean size; as it has been mentioned the shift in size/shape of the GNST brings significant changes in the peak position of tip/core mode plasmons. These resonance bands when close to the central sources used for OCT imaging (central wavelength) produce a very strong interaction, enhancing the backscattered light [45]. However this is not the case, the peak of the tip mode LSPR is at about 810 nm while the central wavelength of this particular clinical IV-OCT is at 1350 nm. As was shown above, one of the ways to obtain effective contrast agents for imaging would then be to increase the mean diameter of the GNST.

However, the increase in size of the nanoparticles brings some pathological concerns in the biological environment that need to be taken in account due to potential health risk. Tough gold nanoparticles are recognized as bio-safe materials and currently researched for biomedical applications such as imaging and targeted drug delivery, studies in mice have revealed that the size plays an important role in their pathological effects on different organs [46]. In the work by Tianmeng Sun, Rachel Simmons, *et al.* [47] the study of the bio distribution of different size gold nanoparticles was performed. It revealed that nanoparticles with a size greater than 5 nm mostly accumulated in the spleen and liver. This organs, from the reticuloendothelial system are responsible for rapid removal of the particles from circulation and are one of the physiological barriers that limits the journey of the nanoparticles [48]. However, in this organs, significant pathological changes to their architecture where reported [46], preventing them from being recognized as safe for intervascular contrast agents.

On the whole, gold nanostars are an obvious choice due to their amenability of synthesis and functionalization, yet they are not good for OCT at this wavelength and not for human use. Therefore, efforts shifted to a different type of contrast agents, the PBCA microbubbles.

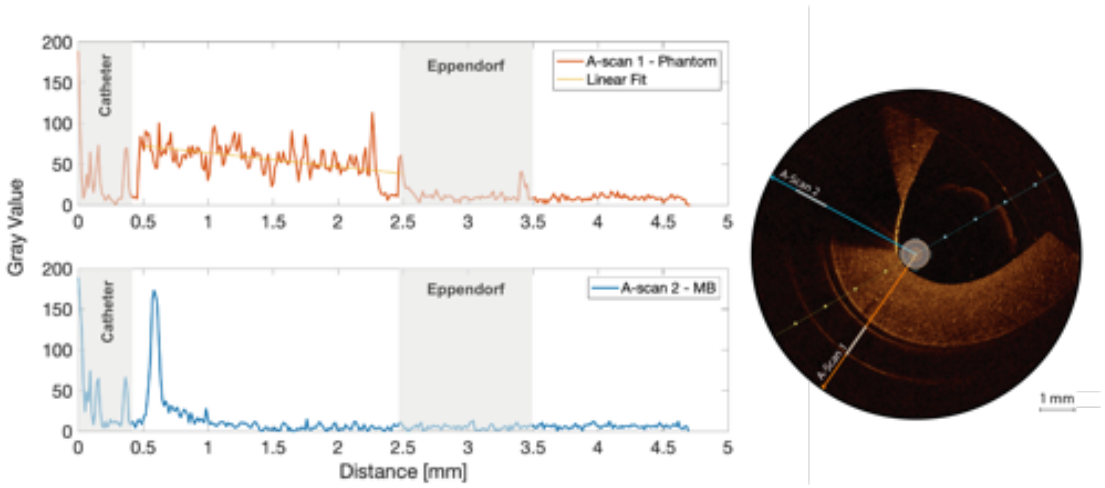

Figure 3.13: Profile of double layer phantoms. Two profile plots are represented. One of the regular phantom (A-scan 1) the other in a region with MB (A-scan 2).

A drop containing 2.8 µm microbubbles was placed in the surface of the phantom as shown in Figure 3.11. Notice the difference between the regions of the phantom in Figure 3.12-(E). A microbubble (MB) layer appears as a highly scattering line, creating a shadow. The signal provided by the microbubbles has a dual characteristic (creates a shadow and shows high reflectivity) that allows its unequivocal location in the sample. In order to further visualize the characteristic signal of the microbubbles, two distinct A-scans from Figure 3.12 were analyzed in Figure 3.13. The gray values were obtained radially to center of the OCT images until a distance of 5 mm from the catheter. The initial gray value peaks, identical in both profiles, correspond to the profile of the imaging catheter. From a region starting 0.5 mm to 2.5 mm the differences are then clearly visible between the normal phantom (A-scan 1) and a region where the MB are present (A-scan 2).

In the phantom the scattering decays constantly due to the extinction of the light beam as the imaging depth increases. The noise observed in the graph is referred to as speckle noise and is characteristic to all coherent imaging systems. It is caused by the interference of light scattered from multiple points within the turbid phantom [49]. On the other hand, the profile obtained in the region with microbubbles presents a different scenario. A narrow high intensity peak is observed followed by an exponential decay of the gray values. This "hypersignal" given by the 2.8 µm microbubbles arises from the refractive index mismatch between the gas-filled MB and the surrounding medium. As the refractive index mismatches increase the scattering increases.

In light of the drawbacks presented for the GNST, microbubbles [MB; currently U. S. Food and Drug Administration (FDA) approved intravascular contrast agents in diagnostic ultrasound [27]] may be a great alternative contrast agent. No other structure in OCT imaging appears has the "shadowed" signal presented by these layer of microbubbles. The only relatable behaviour is that from the struts of a stent that are distributed homogeneously and lie against the intima. In this case the high reflection of the OCT light beam is due to the metal struts, which also cast strong shadows dorsally (Figure 3.14).

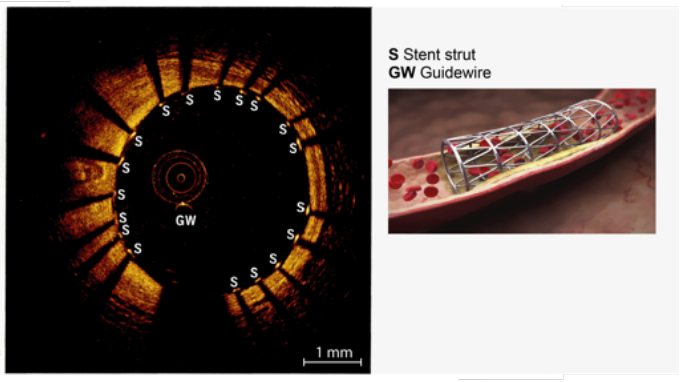

Figure 3.14: OCT cross-section of a stented artery section. Adapted from OCT Compendium by Holger Nef and Albrecht Elsässer [50] and Science Picture Co stock photos.

Following, a Matlab script was created so that the cylindrical dataset resultant of each OCT pullback could be analyzed in its whole. As so, each of the radial images that composes this dataset was initially individually "unwrapped" *e.g.* The input RGB color image (cartesian space) is converted to 16-bit grayscale and remaped with polar coordinates. The remaped images correspond to the set of radial A-scans that compose the image for each angle (1º to 360º) (Figure 3.15-B). For a given remaped image the intensity values along each A-scan are summed. The results are then plotted for all the slices of the OCT pullback. The outcome effectively projects the attenuation and backscatter in a "carpet view" of the entire sample (Figure 3.15-C)

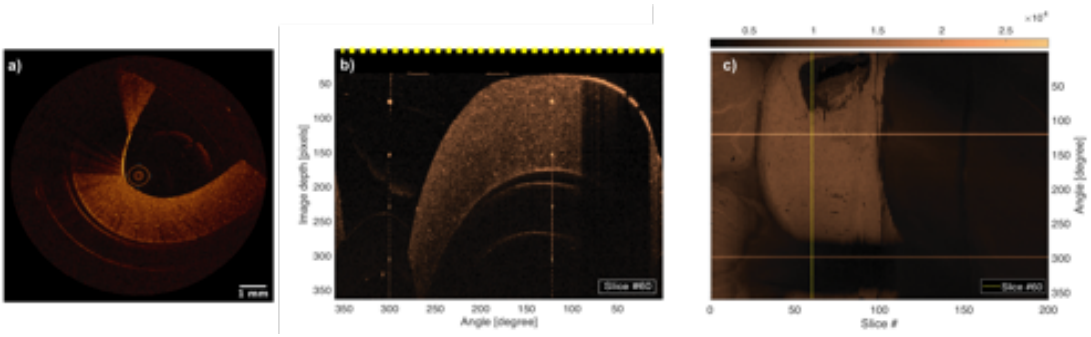

Figure 3.15: a) OCT cross-section of a initial optical phantom were MB contrast is visible, followed by b) the respective unwrapped image and the c) carpet view from all the cross-section taken in the OCT pull-back.

The placement and shape of the drop of MB is then clearly visible as a region where the total intensity value is lower than the surrounding area. This reflects the entire portion that is "shadowed" dorsally to the MB layer. Although the overall shape of the drop is that of a circle, certain regions within this shape have different gray value intensities. This is due to the heterogeneous distribution of the MBs. Denser areas, where the MB are largely accumulated cast an intense shadow since light is more efficiently scattered. Whereas areas less populated still allow some of the light to pass trough. This result has important implications such as the limit of detection of different MB concentrations.

Therefore some tests were carried out trying to vary the total amount of MB in a controlled area. Squares with 0.5 cm side, placed at an equal distance from each other (0.5 cm), were delimited using duct tape. The tape served as a mask for the later N_2 plasma activation of the PDMS surface. The exposed surface then became hydrophilic unlike the remaining PDMS. This step was performed in hopes of containing the MB solution drop in the stipulated area.

Three different quantities of MB were used. Initially the amount of 2 µm MB to cover the $(0.5cm)^2$ surface was calculated: $\approx 6.25 \times 10^6$ MB. It was then defined that from the stock MB solution (3.3×10^9 MB/mL) 2 µL where going to be used in the first square (6.6×10^6 MB). From here on the stock solution was sequentially diluted. The following

square had the stock solution diluted in Triton in a ratio of 1:4, from this 2 µL were used (1.65×10^6 MB). The late solution was again diluted 10-fold (1:40 of the stock solution) and 2 µL where removed (1.65×10^5 MB). Each of the MB solutions was placed in the respective square and left to dry while the entire PDMS slab was oscillating in a lab shaker. This step was carried out in order to achieve an homogeneous distribution of the MB throughout the specified area. The optimized double layer phantom referred in Section 3.1.2 was also used in this tests. The OCT images and their respective treatment are present in Figure 3.16.

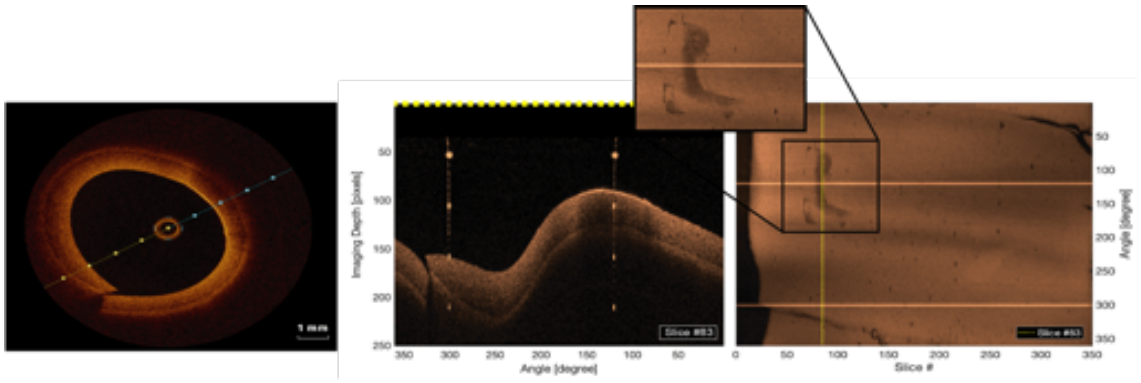

Figure 3.16: OCT cross-section of a double PDMS layer optical phantom with MB shadowing effect, followed by the respective unwrapped image and the carpet view from all the cross-section taken in the OCT pull-back.

Even tough preventive steps were taken to assure a better distribution of the MB in the required area, the visual inspection of the "carpet view" of the sample indicates the clustering of the MB. The inset in Figure 3.16 represents one of the sample areas where the MB were deposited. Most likely correspondent to the stock solution (6.6×10^6 MB) since the MB deposition was performed sequentially from the most concentrated to the less concentrated. Furthermore, no other "shadowed" regions where visible throughout the sample.

The MB as in the immobilization of the GNST in section 3.2.1 should have been functionalized with the surface of the PDMS. In fact some strategies for the immobilization of the MB in the PDMS surface were considered and even tested. One of this options was the MB-shell functionalization process reported by P. Koczera *et al.* [30]. In their work the MB are coupled with streptavidin using EDC (i.e N-(3-dimethylaminopropyl)-N-ethylcarbodiimide hydrochloride) coupling chemistry. This process is the most common technique for the labeling and crosslinking of carboxylic acids to primary amines [51]. With this in mind, the idea was to use EDC chemistry in order to crosslink the MB with the primary amine of the silanized PDMS used in the GNST immobilization (Section 3.2.1). However, following the method described by P. Koczera *et al.* the MB solution had to be initially partly hydrolyzed by increasing the pH to around 10, which in the

tests performed in this work always lead to the instability of the MB and their dissolution. This is believed to be mostly due to the lack of precise methods to tune the pH, which leads to the rapid variation of the values. Thus, without the successful hydrolyzation the butyl-ester groups of the PBCA side chains no resulting carboxyl groups were available for the following EDC process and the immobilization of the MB was not attained.

Nonetheless the evaluation of the optimized double layer phantom was still performed. In a brief comparison of a OCT image of the devised phantom (Figure 3.16) with one of a normal coronary artery (Figure 3.17) the similarities are clearly visible. In both images the layers are easily distinguished by different scattering intensities and the overall shape fits the radial profile of a normal artery. Furthermore, two A-scans from the double layer phantom where recorded from a region with and without MB and the results are present in Annex VI.

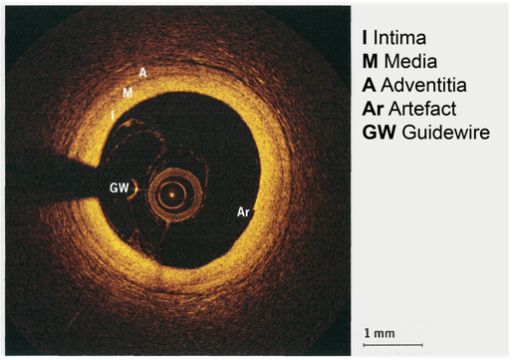

Figure 3.17: Normal coronary artery. Adapted from: OCT Compendium by Holger Nef and Albrecht Elsässer [50]

To evaluate the effects of microbubbles on OCT images of blood vessels, *post mortem* human carotids were imaged with OCT. Using an optimized method for OCT image acquisition (Figure 3.18) the sectioned arteries where fixed in position allowing for a undisturbed OCT pullback.

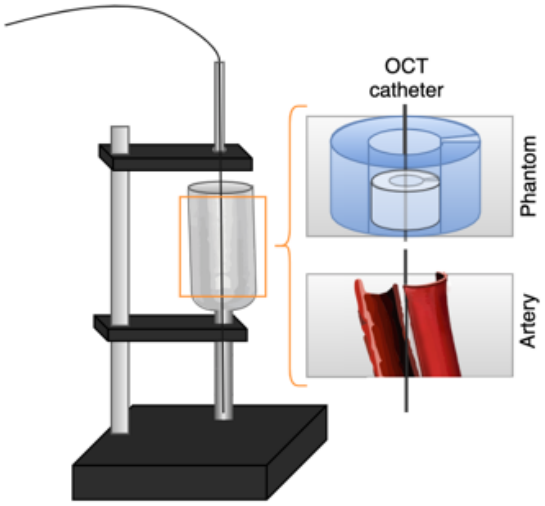

Figure 3.18: OCT setup allowing the fix of both phantoms and arteries while testing. Image designed in Adobe Illustrator®and draw.io [Browser-based end-user diagramming application] (2019).

One of the sections of the artery was incubated with the Target-Ready microbubbles that had been functionalized with anti-VE-Cadherin IgG antibodies and was referred as the positive control (+MB). While the negative control was only immersed in a PBS blocking solution.

Vascular endothelial - cadherin (VE-CAD), also called 7B4 and cadherin-5, belongs to the class of cell adhesion molecules called cadherins [52]. Cadherins play a role in tissue formation and help maintain tissue architecture in the adult [53]. VE-cadherin, more specifically is located at endothelial junctions [54], and was chosen precisely because of this location. The endothelial cells line the interior surface of blood vessels and biomarkers in this region would provide the closest comparison with the tests in the phantom samples. Furthermore, the endothelial lining is involved in inflammatory responses as in the case of atherosclerosis [55]. The arteries used in this work had been previously confirmed for the presence of the endothelial cells in a immunohistochemistry process performed by the group at INL. A selected OCT image and the respective remapping is present in Figure 3.19.

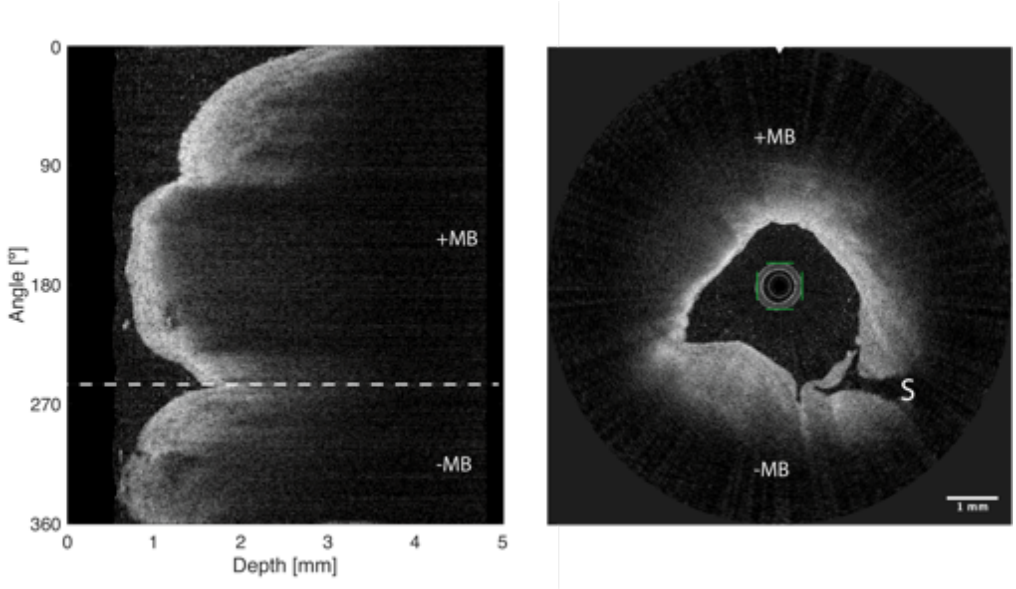

Figure 3.19: OCT cross-section and respective unwraped image of two sections of human carotid artery. +MB: Artery section incubated with targeted MB; -MB: artery section incubated in blocking solution; S: separation between the two artery sections.

For the morphological analysis of the OCT Scan the principles of interpretation of such exams can be applied. As so, some steps are usually undertaken in order to obtain the best classification scheme. Initially one should inquire if there are any abnormalities in the vessel walls. Which besides the region where both sections of the artery are separated only irregular reflection and attenuation profiles are noticed in the +MB. Following, analyzing the brightness and the shadows it is possible to guess the type of tissue and the structures. In the -MB section no shadows, bright areas or dark spots are visible which is

correspondent to the normal signal of a vessel wall.

However, in the artery section where the MB were incubated the signal appears to be heterogeneous. Some regions exhibit thin bright bands at the surface facing the OCT catheter followed by pronounced shadows. This type of profiles are usually associated either to stents or thrombus regions (Table 3.3). Yet, none of this structures could have been present in the samples as so it is assumed that these are regions where MB have successfully binded with endothelial biomarkers. In fact the MB shadowing effect and hypersignal reported before is clearly visible.

Table 3.3: Identification of the tissue and the structures using reflection and attenuation. Adatpted from: OCT Compendium by Holger Nef and Albrecht Elsãsser [50]

Reflection and attenuation	**Strong reflection (bright area)**	**Weak reflection (dark area)**
Strong attenuation (strong shadows)	Bright area, strong shadows, e.g. stent, red thrombus **Stent**: Attenuation due to reflection and absorption **Thrombus**: Attenuation due to reflection and absorption	Dark area, strong shadows, e.g. lipid Attenuation due to absorption
Weak attenuation (weak shadows)	Bright area, hardly any shadows, e.g. fibrous tissue	Dark area, hardly any shadows, e.g. plaque

The "carpet view" of the OCT pullback was obtained using the designed MATLAB script and is represented in Figure 3.20 side by side with a picture of the respective artery sections. The location of the cross-section in Figure 3.19 is represented by the yellow line in the "carpet view". Furthermore, the regions that corresponded to the behaviour described above (Strong shadows and bright area) are delimited by a white dashed line.

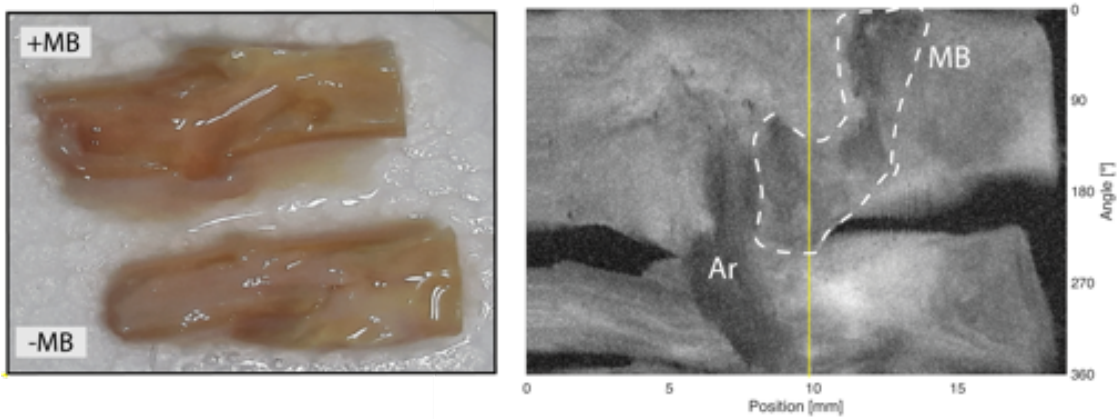

Figure 3.20: Carpet view from the artery sections OCT pull-back. **-MB**: Artery section incubated with targeted MB; **-MB**: artery section incubated in blocking solution; **Ar**: Artifact

The effect of the MB is substantial, the region where they are present is able to be easily distinguished from the surrounding tissue. Only some image artifacts from the OCT catheter leaning against the artery walls create darkened spots that can be easily dismissed by observing the respective cross-sections at the given pullback length.

However having used MB targeted for endothelial cells one might ask why are the MB confined to certain regions and not the entire lining of the artery. The thing is that investigation of the endothelial layer may be hampered since it is a very fragile structure that can be destroyed trough all the handling steps of the sample. Leaving only small sections of endothelial cells.

Advances in MB functionalization can enable the incorporation of various targeting ligands. Instead of general VE-cadherin endothelial biomarker, specific targets that reflect vulnerable plaque progression can be used to track the disease. As a matter of fact a whole research area is dedicated solely into understanding which molecular medical signs are unique to vulnerable plaques [56].

Focal manifestations of atherosclerosis such as inflammation and endothelial activation are potentially the most direct approach to disease biomarkers. As so, biomarkers for pro-inflammatory cytokines (IL-6, IL-1β, TNF-α) and acute-phase reactants (CRP, PTX3) or even cell adhesion molecules (ICAM-1, VCAM-1, E-Selectin) [56, 57] would be candidates for future targeted MB.

The otherwise poor personalized risk assessment and guided treatment [58] could then be mitigated by an accurate vulnerable plaque location and quantification. In fact one of the main advantages of the MB referred by the partner physicians in both Braga and Vigo Hospital would be in guiding interventional procedures such as stent placement. Pre-emptively increasing the stented region into surrounding vulnerable plaques (when present) could potentially reduce the risk of stent-caused acute cases from induced strains. This is an example of a risk-factor–reducing strategy that can be implemented with vulnerable plaque prediction.

Chapter 4

Conclusion and Future Perspectives

The ability to survey the distribution of a biochemical species within a biological sample provides an essential dimension of information beyond the tissue morphology obtained in current optical coherence tomography setups. However, as a first step, molecular-specific exogenous contrast agents needed to be identified and investigated. Doing so, some of the pertinent questions in the field were addressed in this work: (1) Can contrast agents be easily prototyped before being tested in actual living tissues? (2) How do we engineer some of the contrast agents to optimize on their contrast rendering capability? (3) How do we functionalize the contrast agents so that they can bind to a biochemical species of interest?

In this study we find a faint increase in intensity of the OCT signal in areas containing GNST. Showing that gold nanostar-shaped nanoparticles where not the best option for OCT imaging as size limitations eliminate the possibility of tuning the LSPR peaks into the working wavelength of most clinical OCTs without consequent pathological effects. As so, in order to obtain plasmon-resonant contrast agents, more efficient structures or even different materials should be investigated to obtain an increased scattering effect at the working wavelength of most OCT systems ($\approx 1300nm$) without significantly increasing their size.

The gold nanoparticles were however successfully immobilized and patterned in the designed tissue-mimicking phantom. A process that could be of great importance in testing different types of contrast agents, allowing a case-by-case study of their qualitative signal as a marker for the expression of surface receptors without the difficulty of constantly arranging *post mortem* arteries that aren't always available and that require a lot more preparation.

Conversely, it is suggested that targeted-microbubbles are interesting candidates for increasing sensitivity in OCT diagnosis of vulnerable plaques because MB not only significantly enhance OCT contrast but provide an unequivocal signal from all different types of structures in human arteries. Moreover, the fact that this type of contrast agent is already approved for intervascular use in ultrasound imaging techniques facilitates its adaptation to this new type of modality. Each imaging method differs from another in terms of resolution, imaging depth and sample intrusiveness. As so, on many occasions it is important to complement prognosis with different imaging modalities. The development of multimodal contrast agents such as the presented PBCA microbubbles is therefore considered to be highly advantageous in improving patient care and reducing the number of contrast agents administrations. This should encourage future trials exploring not only diagnostic accuracy of MB in OCT imaging but also look into the specific molecular targets to be functionalized on their surface.

Future perspectives

A further research objective will include the optimization of the imaging protocol for the *post mortem* human arteries by adding pre and post microbbubble contrast agent incubation images which should allow to unambiguously associate the signal to the MB and not any other structures or image artifacts.

Further detailed characterisation of the microbbubles will be gained by continuous analysis of samples, namely the limits of detection using OCT, varying the different concentrations of microbubbles especially if the successfull Phantom PDMS immobilization of this contrast agents is attained. The PDMS immobilization will allow for faster and more precise quantification of the microbbuble signal using OCT.

The initial testing of different biomarkers attached to the MB, more specific to atherosclerotic process should also be taken into consideration. Biomarkers such as the referred pro-inflammatory cytokines (IL-6, IL-1, TNF-) and acute-phase reactants (CRP, PTX3) or even cell adhesion molecules (ICAM-1, VCAM-1, E-Selectin).

Furthermore, the antibody to microbbuble functionalization process, based in the biotin streptavidin interaction, should also be reviewed since actual *in vivo* application would most certainly lead to nonspecific antibody binding since streptavidin would bind to the already present biotin in the human body.

Finally the creation of a lumen segmentation algorithm, that would delimit the profile of the artery walls, could be used to further perfect the MATLab script created for the projection of the artery pull back. In turn, allowing for a increase in the "carpet view" (3D view of the artery) contrast in regions with microbbubbles, since it would allow for a better control over the sections being summed to obtain this image.

Bibliography

[1] World Health Organization. *World health statistics 2018: monitoring health for the SDGs, sustainable development goals*. Tech. rep. 2018, p. 100.

[2] H. Thomas, J. Diamond, A. Vieco, S. Chaudhuri, E. Shinnar, S. Cromer, P. Perel, G. A. Mensah, J. Narula, C. O. Johnson, G. A. Roth, and A. E. Moran. "Global Atlas of Cardiovascular Disease 2000-2016: The Path to Prevention and Control." In: *Global Heart* 13.3 (2018), pp. 143–163.

[3] J. Ralston. "Management Matrix 25 X 25 : Reducing Premature Mortality from Cardiovascular Disease." In: *Radiology Management, ICU Management, Healthcare IT, Cardiology Management, Executive Management* 15.3 (2015).

[4] C. Costa Oliveira and M. Brito. "How to Look Closely to Vulnerable Atherosclerotic Plaques Using Nanoparticles." In: *Journal of Nanomedicine Research* 6.1 (2017).

[5] D. Huang, E. A. Swanson, C. P. Lin, J. S. Schuman, W. G. Stinson, W. Chang, M. R. Hee, T. Flotte, K. Gregory, C. A. Puliafito, J. G. Fujimoto, C. P. Lin, J. S. Schuman, and C. A. Puliafito. "Optical Coherence Tomography HHS Public Access." In: *Science* 254.5035 (1991), pp. 1178–1181.

[6] D. P. Popescu, L. P. Choo-Smith, C. Flueraru, Y. Mao, S. Chang, J. Disano, S. Sherif, and M. G. Sowa. "Optical coherence tomography: Fundamental principles, instrumental designs and biomedical applications." In: *Biophysical Reviews* 3.3 (2011), pp. 155–169.

[7] Z. Chen and G. Liu. "Doppler optical coherence tomography." In: *Handbook of Coherent-Domain Optical Methods: Biomedical Diagnostics, Environmental Monitoring, and Materials Science:: Second Edition* 2-2 (2013), pp. 889–922.

[8] B. Baumann. "Polarization Sensitive Optical Coherence Tomography: A Review of Technology and Applications." In: *Applied Sciences* 7.5 (2017), p. 474.

[9] M. Yamanaka, N. Hayakawa, and N. Nishizawa. "High-spatial-resolution deep tissue imaging with spectral-domain optical coherence microscopy in the 1700-nm spectral band." In: *Journal of Biomedical Optics* 24.07 (2019), p. 1.

[10] D. Hillmann, C. Pfäffle, H. Spahr, S. Burhan, L. Kutzner, F. Hilge, and G. Hüttmann. "Computational adaptive optics for optical coherence tomography using multiple randomized subaperture correlations." In: *Optics Letters* 44.15 (Aug. 2019), p. 3905.

[11] G. J. Lu, L.-d. Chou, D. Malounda, A. K. Patel, D. S. Welsbie, and D. L. Chao. "Biomolecular Contrast Agents for Optical Coherence Tomography." In: *bioRxiv* (Mar. 2019), pp. 1–9.

[12] M. Varna, H. V. Xuan, and E. Fort. "Gold nanoparticles in cardiovascular imaging." In: *Wiley Interdisciplinary Reviews: Nanomedicine and Nanobiotechnology* 10.1 (Jan. 2018), e1470.

[13] R. S. Fenning and R. L. Wilensky. "New insights into the vulnerable plaque from imaging studies." In: *Current Atherosclerosis Reports* 16.3 (2014), pp. 1–9.

[14] N. R. Shah. "Optical Coherence Tomography in Coronary Atherosclerosis." In: *MOJ Anatomy & Physiology* 1.1 (2016), pp. 11–14.

[15] B. E. Bouma, S.-H. Yun, B. J. Vakoc, M. J. Suter, and G. J. Tearney. "Fourier-domain optical coherence tomography: recent advances toward clinical utility." In: *Current Opinion in Biotechnology* 20.1 (Feb. 2009), pp. 111–118.

[16] A. S.F. C. Silva and A. L. Correia. "From optical coherence tomography to Maxwell's equations." In: *2013 IEEE 3rd Portuguese Meeting in Bioengineering (ENBENG)*. September. IEEE, Feb. 2013, pp. 1–4.

[17] P. M.d. S. Carvalho. "OPTICAL COHERENCE TOMOGRAPHY Layout Simulation using MATLAB ®." Doctoral dissertation. Universidade de Coimbra, 2016, p. 136.

[18] P. Serranho, A. M. Morgado, and R. Bernardes. "Optical Coherence Tomography: A Concept Review." In: 2012, pp. 139–156.

[19] V. V. Tuchin. "Tissue Optics and Photonics: Biological Tissue Structures." In: *Journal of Biomedical Photonics & Engineering* 1.1 (2015), pp. 3–21.

[20] A. A. Serafetinides, M. Makropoulou, and E. Drakaki. "Biophotonics in diagnosis and modeling of tissue pathologies." In: *15th International School on Quantum Electronics: Laser Physics and Applications* 7027.December (2008), p. 702715.

[21] L. A. Sordillo, Y. Pu, S. Pratavieira, Y. Budansky, and R. R. Alfano. "Deep optical imaging of tissue using the second and third near-infrared spectral windows." In: *Journal of Biomedical Optics* 19.5 (2014), p. 056004.

[22] J. G. Fujimoto, S. A. Boppart, G. J. Tearney, B. E. Bouma, C Pitris, and M. E. Brezinski. "High resolution in vivo intra-arterial imaging with optical coherence tomography." In: *Heart* 82.2 (Aug. 1999), pp. 128–133.

[23] C. Yang. "Molecular Contrast Optical Coherence Tomography: A Review." In: *Photochemistry and Photobiology* 100.2 (2004), pp. 130–134.

[24] C. Yang, M. A. Choma, L. E. Lamb, J. D. Simon, and J. A. Izatt. "Protein-based molecular contrast optical coherence tomography with phytochrome as the contrast agent." In: *Optics Letters* 29.12 (2004), p. 1396.

[25] S. A. Boppart, A. L. Oldenburg, C. Xu, and D. L. Marks. "Optical probes and techniques for molecular contrast enhancement in coherence imaging." In: *Journal of Biomedical Optics* 10.4 (2005), p. 041208.

[26] J. K. Barton, J. B. Hoying, and C. J. Sullivan. "Use of microbubbles as an optical coherence tomography contrast agent." In: *Academic Radiology* 9.SUPPL. 1 (2002), pp. 52–55.

[27] H. Assadi, V. Demidov, R. Karshafian, A. Douplik, and I. A. Vitkin. "Microvascular contrast enhancement in optical coherence tomography using microbubbles." In: *Journal of Biomedical Optics* 21.7 (July 2016), p. 076014.

[28] P. Senthil Kumar, I. Pastoriza-Santos, B. Rodríguez-González, F. Javier García De Abajo, and L. M. Liz-Marzán. "High-yield synthesis and optical response of gold nanostars." In: *Nanotechnology* 19.1 (2008).

[29] J. Turkevich, P. C. Stevenson, and J. Hillier. "A study of the nucleation and growth processes in the synthesis of colloidal gold." In: *Discussions of the Faraday Society* 11.c (1951), p. 55.

[30] P. Koczera, L. Appold, Y. Shi, M. Liu, A. Dasgupta, V. Pathak, T. Ojha, S. Fokong, Z. Wu, M. van Zandvoort, O. Iranzo, A. J. Kuehne, A. Pich, F. Kiessling, and T. Lammers. "PBCA-based polymeric microbubbles for molecular imaging and drug delivery." In: *Journal of Controlled Release* 259 (Aug. 2017), pp. 128–135.

[31] N. B. Trung, H. Yoshikawa, E. Tamiya, P. H. Viet, Y. Takamura, and T. Ashahi. "Propitious immobilization of gold nanoparticles on poly(dimethylsiloxane) substrate for local surface plasmon resonance based biosensor." In: *Japanese Journal of Applied Physics* 51.3 PART 1 (2012).

[32] D. Nunes, A. Pimentel, L. Santos, P. Barquinha, E. Fortunato, and R. Martins. "Photocatalytic TiO2 Nanorod Spheres and Arrays Compatible with Flexible Applications." In: *Catalysts* 7.12 (2017), p. 60.

[33] C.- Bisaillon, M. L. Dufour, and G. Lamouche. "Artery phantoms for intravascular optical coherence tomography: healthy arteries." In: *Biomedical Optics Express* 2.9 (2011), p. 2599.

[34] G. Lamouche, B. F. Kennedy, K. M. Kennedy, C.-E. Bisaillon, A. Curatolo, G. Campbell, V. Pazos, and D. D. Sampson. "Review of tissue simulating phantoms with controllable optical, mechanical and structural properties for use in optical coherence tomography." In: *Biomedical Optics Express* 3.6 (2012), p. 1381.

[35] D. K. Cai, A. Neyer, R. Kuckuk, and H. M. Heise. "Optical absorption in transparent PDMS materials applied for multimode waveguides fabrication." In: *Optical Materials* 30.7 (2008), pp. 1157–1161.

[36] A. Kedia and P. S. Kumar. "Gold nanostars reshaping and plasmon tuning mechanism." In: *AIP Conference Proceedings* 1512.February 2013 (2013), pp. 232–233.

[37] W. Lv, C. Gu, S. Zeng, J. Han, T. Jiang, and J. Zhou. "One-pot synthesis of multibranch gold nanoparticles and investigation of their SERS performance." In: *Biosensors* 8.4 (2018).

[38] C. G. Khoury and T. Vo-Dinh. "Gold Nanostars For Surface-Enhanced Raman Scattering: Synthesis, Characterization and Optimization." In: *The journal of physical chemistry. C, Nanomaterials and interfaces* 2008.112 (2008), pp. 18849–18859.

[39] O. Bibikova. "Plasmon-resonant gold nanoparticles for bioimaging and sensing applications." Doctoral dissertation. UNIVERSITY OF OULU, 2018, pp. 32–112.

[40] T. Hendel, M. Wuithschick, F. Kettemann, A. Birnbaum, K. Rademann, and J. Polte. "In situ determination of colloidal gold concentrations with uv-vis spectroscopy: Limitations and perspectives." In: *Analytical Chemistry* 86.22 (2014), pp. 11115–11124.

[41] X. Liu, M. Atwater, J. Wang, and Q. Huo. "Extinction coefficient of gold nanoparticles with different sizes and different capping ligands." In: *Colloids and Surfaces B: Biointerfaces* 58.1 (2007), pp. 3–7.

[42] L. Scarabelli, M. Grzelczak, and L. M. Liz-Marzán. "Tuning gold nanorod synthesis through prereduction with salicylic acid." In: *Chemistry of Materials* 25.21 (2013), pp. 4232–4238.

[43] T. Yokoyama and T. Kinoshita. "High-performance liquid chromatographic determination of biotin in pharmaceutical preparations by post-column fluorescence reaction with thiamine reagent." In: *Journal of Chromatography A* 542.C (1991), pp. 365–372.

[44] T. Miron and M. Wilchek. "A spectrophotometric assay for soluble and immobilized N-hydroxysuccinimide esters." In: *Analytical Biochemistry* 126.2 (1982), pp. 433–435.

[45] Y. Ponce De León, J. L. Pichardo-Molina, N. Alcalá Ochoa, and D. Luna-Moreno. "Contrast enhancement of optical coherence tomography images using branched gold nanoparticles." In: *Journal of Nanomaterials* 2012 (2012).

[46] K. E. Ibrahim, M. G. Al-Mutary, A. O. Bakhiet, and H. A. Khan. "Histopathology of the liver, kidney, and spleen of mice exposed to gold nanoparticles." In: *Molecules* 23.8 (2018).

[47] T. Sun, R. Simmons, D. Huo, B. Pang, X. Zhao, C. W. Kim, H. Jo, and Y. Xia. "Targeted delivery of anti-miR-712 by VCAM1-binding Au nanospheres for atherosclerosis therapy." In: *ChemNanoMat* 2.5 (2016), pp. 400–406.

[48] B. Sutapa and M. Samir. "Challenges associated with Penetration of Nanoparticles across Cell and Tissue Barriers: A Review of Current Status and Future Prospects." In: *Nano Today* 9.2 (2014), 223–243.

[49] I. Freund and Isaac. "Joseph W. Goodman: Speckle Phenomena in Optics: Theory and Applications." In: *Journal of Statistical Physics* 130.2 (Nov. 2007), pp. 413–414.

[50] P. D.m. H. Nef and P. D.m. A. Elsãsser. *OCT Compendium*. 1st. Giessen, Germany, 2016, p. 72.

[51] M. J. Fischer. "Amine coupling through EDC/NHS: a practical approach." In: *Methods in molecular biology (Clifton, N.J.)* 627 (2010), pp. 55–73.

[52] M. Takeichi. "Cadherin cell adhesion receptors as a morphogenetic regulator." In: *Science* 251.5000 (1991), pp. 1451–1455.

[53] P Carmeliet, M. G. Lampugnani, L Moons, F Breviario, V Compernolle, F Bono, G Balconi, R Spagnuolo, B Oosthuyse, M Dewerchin, A Zanetti, A Angellilo, V Mattot, D Nuyens, E Lutgens, F Clotman, M. C. de Ruiter, A Gittenberger-de Groot, R Poelmann, F Lupu, J. M. Herbert, D Collen, and E Dejana. "Targeted deficiency or cytosolic truncation of the VE-cadherin gene in mice impairs VEGF-mediated endothelial survival and angiogenesis." In: *Cell* 98.2 (July 1999), pp. 147–57.

[54] V. M. Braga, A. Del Maschio, L. Machesky, and E. Dejana. "Regulation of cadherin function by Rho and Rac: Modulation by junction maturation and cellular context." In: *Molecular Biology of the Cell* 10.1 (1999), pp. 9–22.

[55] A. R. Pries, T. W. Secomb, and P. Gaehtgens. "The endothelial surface layer." In: *Pflugers Archiv European Journal of Physiology* 440.5 (2000), pp. 653–666.

[56] G. Lammeren, F. L. Moll, G. Jan, D. Borst, D. Kleijn, J. Vries, and G. Pasterkamp. "Atherosclerotic plaque biomarkers : beyond the horizon of the vulnerable plaque." In: *Current Cardiology Reviews* 7 (2011), pp. 22–27.

[57] T. Soeki, T. Niki, K. Kusunose, S. Bando, Y. Hirata, N. Tomita, K. Yamaguchi, K. Koshiba, S. Yagi, Y. Taketani, T. Iwase, H. Yamada, T. Wakatsuki, M. Akaike, and M. Sata. "Elevated concentrations of pentraxin 3 are associated with coronary plaque vulnerability." In: *Journal of Cardiology* 58.2 (2011), pp. 151–157.

[58] C. Stefanadis, C.-K. Antoniou, D. Tsiachris, and P. Pietri. "Coronary Atherosclerotic Vulnerable Plaque: Current Perspectives." In: *Journal of the American Heart Association* 6.3 (Mar. 2017), p. 18.

Nanostars synthesis

Citrate stabilized gold nanoparticles will be synthesized by using the Turkevich method [29].

Reagents:

- Aqua regia – for glassware cleaning (1 Volume of nitric acid (HNO_3) and 3 volumes of hydrochloric acid (3 HCl) are mixed).
- $HAuCl_4$ x $3H_2O$
- Sodium citrate dihydrate
- Milli-Q water

Procedure:
Gold citrate nanoparticles synthesis:

1. 100 mL of 0.5 mM aqueous solution of $HAuCl_4$ under vigorous magnetic stirring and heated boiling.
2. When the mixture from 1 is boiling, quickly add 5 mL of a 1% sodium citrate solution (previously heated to avoid temperature decompensation). Keep heating and stirring until the solution turns from light yellow to dark red (wine appearance).
3. Leave until it reaches room temperature and store in fridge.
4. Calculate the Au concentration with ABS_{400}.

PVP coating of the gold citrate nanoparticles previously synthesized:

- PVP (M.W. 10000 g/mol): We have to coat the gold surface with 60 PVP molecules per nm^2 of gold citrate.
- Magnetic stirring overnight.
- Washing cycle 90 minutes/7000 rpm.
- Remove supernatant and repeat washing cycles of removed supernatant until it's transparent or almost transparent.
- Redisperse in EtOH or isopropanol. You can use the volume that you like to redisperse, but I usually redisperse again in the same starting volume.
- Recalculate the concentration of gold with UV-vis and ABS_{400}.

GNST synthesis:
Based on the reported work by Pandian Senthil Kumar *et al* 2008 Nanotechnology [28].
Reagents:

- Solvent: DMF
- PVP-10000= 10 mM
- $HAuCl_4$= 0.5 mM
- Au-citrate-PVP= 0.8×10^{-3}M GOLD SEEDS (Can change with new synthesis)

Procedure:

1. Dissolve the 10 g PVP in the 100 mL DMF
2. Sonicate 15 min.
3. Under magnetic stirring add the 396.6 µL $HAuCl_4$: (stock concentration=0.12608M) wait around 2 minutes.
4. Under magnetic stirring add the 3.13 mL gold seeds coated with PVP (Au@Citrate@PVP, stock concentration = 0.8×10^{-3} M) and wait 1h or until full reduction is observed – UV-vis and blueish color
5. 3 washing cycles 30 min 4000/4000/4000.
6. Redisperse in isopropanol
7. After the washes (in 25 mL) the last one GNSTs are redispersed in half of the volume (in 12.5 mL).
8. Measurement of the concentration by UV-Vis, ABS_{400}.

GNST and fluorescent dye Codification

1. Put in a falcon 1 mL of GNST at 0.8 mM
   + add 2.7 µL MUA (Mercaptoundecanoic acid) (0.0375 mM) at final concentration 0.1µM
   + TB (Toluidine Blue) and NB (Nile Blue) in final concentration of the 10^{-4} M
   + add 4.3 µL of NH_4OH 29%.
2. Magnetic stirring during 2h.
3. Washing step – centrifuge at 2500 rpm during 30 min, then remove the supernatant and add IPA until 1 mL.

MB biofunctionalization protocol

II.1 Biotin Labeling Reaction

1. Remove the vial of Sulfo-NHS-LC-Biotin from freezer and equilibrate it to room temperature before opening
2. Immediately before use, prepare a 10 mM solution of the biotin reagent. Add 2.78 mg of reagent to 500 µl of ultrapure water in a 0.5 mL eppendorf. Keep 15 µl on a 200 µl eppendorf and label.
3. Dilute 250 µg of antibody stock solution in saline solution for a total volume of 3.750 mL. From the 2.5 mg/mL antibody stock remove 100 µl and add to 3.65 mL of saline. Keep 15 µl on a 200 µl eppendorf and label.
4. Add 10 µl of Biotin (10 mM) to the protein solution
5. Incubate the reaction in ice for 2 hours or at room temperature for 30 min. Keep 15 µl on a 200 µl eppendorf and label.
6. Protein labeling is complete at this point, and although excess non-reacted and hydrolyzed biotin reagent remains in the solution, it is often possible to perform preliminary tests of the labeled protein by Elisa or Western blot. To use use the biotinylated antibodies with the microbubbles the proteins first must be desalted or dialyzed to remove non reacted biotin.

II.2 Antibody filtration

1. In one centrifugal filter add 500 µL of the prepared protein solution.
2. Centrifuge for 10 min at 15k RPM, at room temperature.
3. For this filtering conditions, the Amicon centrifugal filter's user refered that the concentrate solution should have 50 µL of 2/3 mg/mL of protein. Since for the following steps it is required 20 µg of antibody in a total volume of 300 µL, 30 µL of the concentrate solution were added to 0.27 mL of saline.

II.3 Vevo MicroMarker Contrast Agent Conjugated with the Isotype Control Antibody

1. Attach the 21G 5/8" needle to the 1 mL syringe
2. Reconstitute the Target-ready contrast agent from one of the vials by ejecting 0.7 mL of saline.
3. Gently agitate for 10 seconds and let sit at room temperature.
4. Using a 21G 5/8" needle with a 1 mL syringe draw up 0.3 mL of the biotinylated antibody solution prepared before (20 µg biotynilated-Ab in a total volume of 300 µL saline solution). Inject it into the vial of reconstituted Vevo Marker. Total volume 1000 µl
5. Gently agitate the vial by hand for 1 min and let it rest at room temperature for 15

minutes

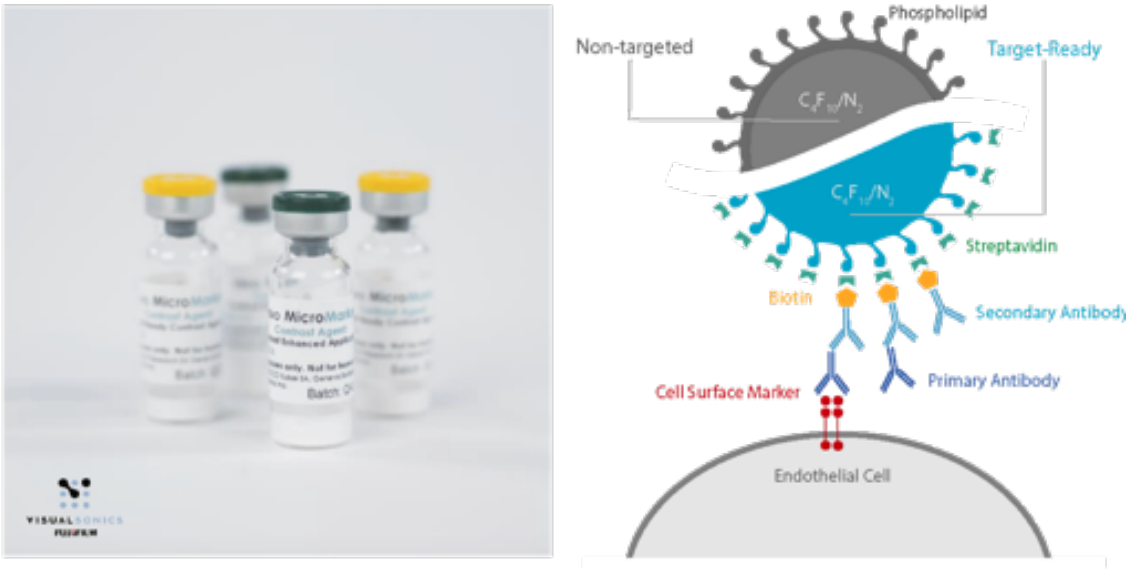

Figure II.1: Lyophilized VeVo MicroMarker® stored in a glass vial. The vial contains a gas head-space consisting of nitrogen (N_2) and perfluorobutane (C_4F_{10}). Graphical representation of Non-targeted and Target-Ready surface-modified microbubbles (MB). Adapted from "Discover Nonlinear Ultrasound Contrast Agent Imaging", FUJIFILM VisualSonics website using Adobe Illustrator®.

Nanostar shape

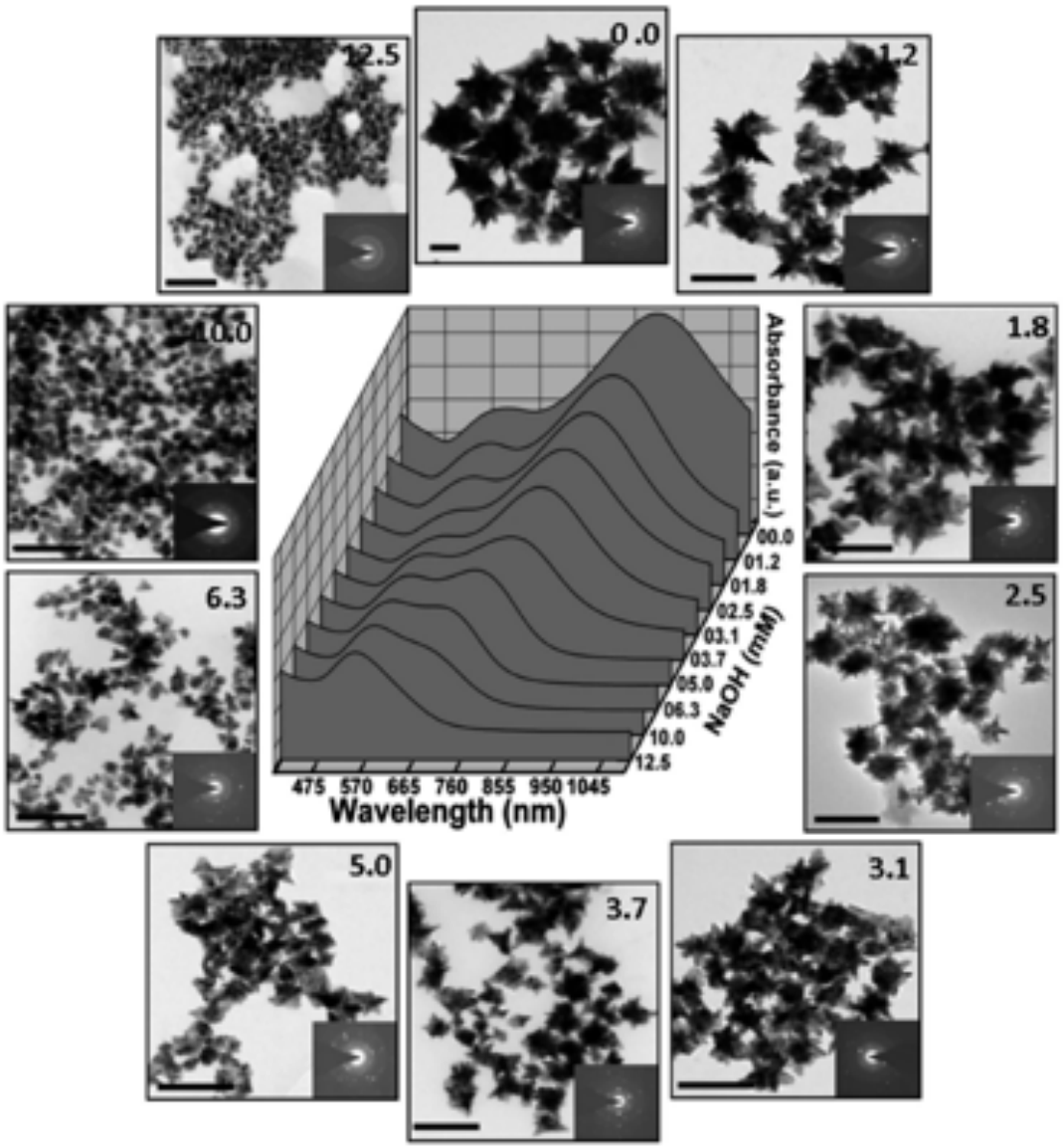

Figure III.1: Optical absorption spectra (centre) showing the effect of the size/shape of GNST in plasmon peak position [36]. The decrease of the GNST tips leads to weaker plasmonic effect and at lower wavelengths.

GNST immobilization APTES

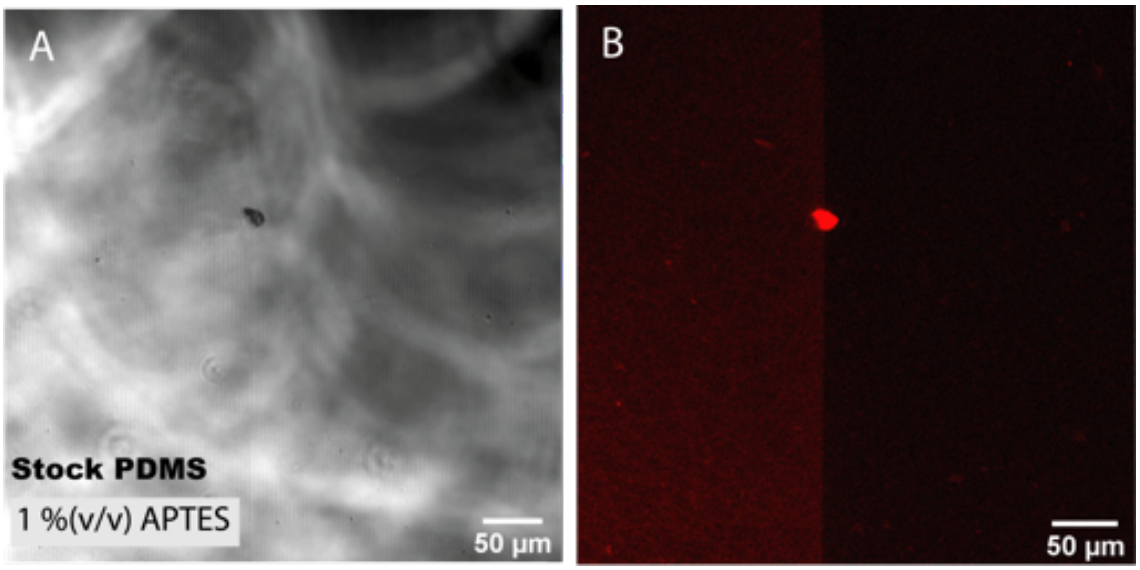

Figure IV.1: Confocal microscope images of functionalized stock PDMS. A)Transmission image,B)Fluorescence image.

Table V.1: BSA concentration in saline solution versus respective absorbance values used in the standard calibration curve.

	BSA Concentration	Measured absorbances			
	mg/mL	Abs1	Abs2	Abs3	**Average**
A	**250**	103	105	105	**104**
B	**125**	43	45	44	**44**
C	**62.5**	23	36	23	**27**
D	**31.3**	4	12	23	**13**
E	**15.6**	2	3	2	**2**
F	**7.8**	1	2	1	**1**
G	**3.9**	1	1	1	**1**
H	**0**	0	0	0	**0**

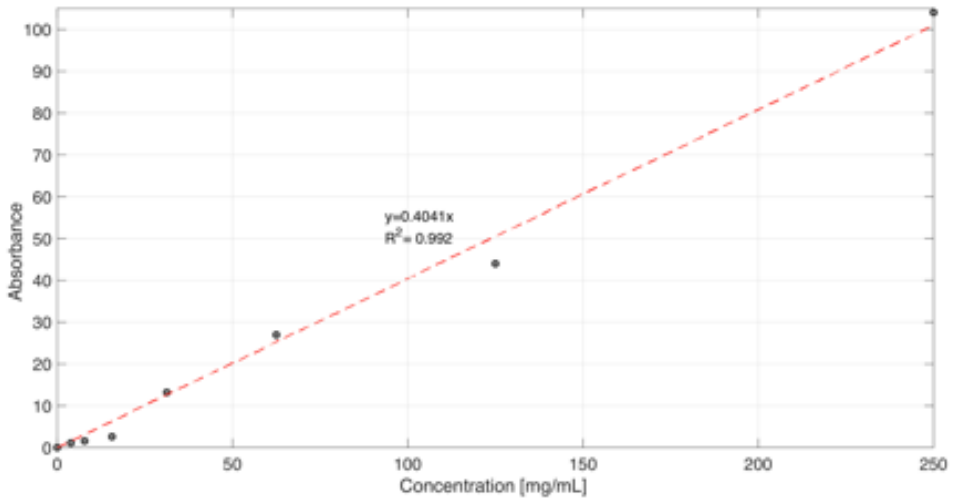

Figure V.1: BSA calibration curve and respective linear fit.

Table V.2: Measured absorbance of the different aliquots from the filtration process and the respective interpolation of the concentration based on the calibration curve.

	Measured absorbance				Concentration
	Abs1	Abs2	Abs3	**Average**	mg/mL
Initial Biotin	2	3	1	**2**	5
Initial Antibody	0.08	0.06	0.07	**0.07**	0.18
Total antibody+biotin	0.30	0.32	0.31	**0.31**	0.77
Concentrated	0.03	0.04	0.05	**0.04**	0.12
Filtered	0.20	0.20	0.20	**0.20**	0.50

OCT A-Scans

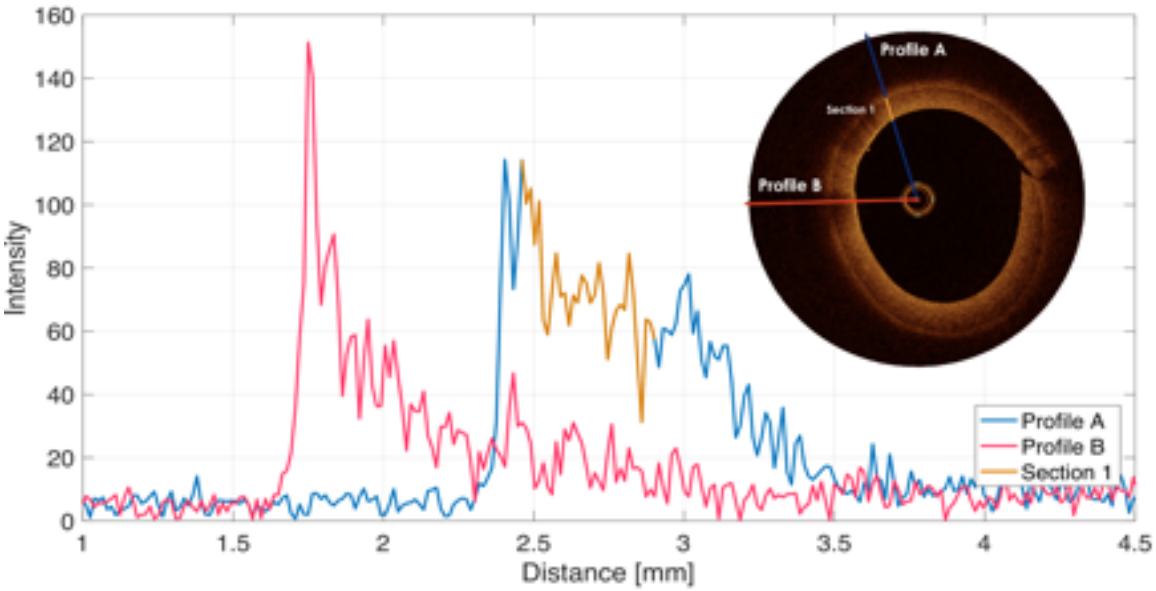

Figure VI.1: Raw profile of double layer phantoms. In profile A, a region without MB, two distinct scattering profiles are noticed from the two layers with different TiO_2 concentrations. The intensity decay is dissimilar between the layers.